Supporting Information for

Electrochemical Oxygen Pump Assisted Solar Thermochemical CO_2 Reduction

Runsen Wang [a, b], Hui Liu [a, b], Yuefan Tuo [a, b], Qi Zhang [a, b], Lei Zhao [a, b], Da Xu [a, b], Yuzhu Chen [a, b], Jieyang Li [a, b], Haojie Zhu [a, b], Xiaoyu Wu [c], Wonjae Choi [c, d], Ziyao Wu [c], Sophia Haussener [e, *], Harry L. Tuller [f, *], Ahmed F. Ghoniem [c, *], and Meng Lin [a, b, *]

[a]Department of Mechanical and Energy Engineering, Southern University of Science and Technology, Shenzhen 518055, P.R. China

[b]SUSTech Energy Institute for Carbon Neutrality, Southern University of Science and Technology, Shenzhen 518055, P.R. China

[c]Department of Mechanical Engineering, Massachusetts Institute of Technology, Cambridge, MA 02139, United States

[d]Division of Mechanical and Biomedical Engineering, Ewha Womans University, South Korea

[e]Laboratory of Renewable Energy Science and Engineering, EPFL, 1015 Lausanne, Switzerland

[f] Department of Materials Science and Engineering, Massachusetts Institute of Technology, Cambridge, MA 02139, United States

*To whom correspondence should be addressed: linm@sustech.edu.cn.

Content

S1 Development of the prediction model and results

S1.1 Model Development

To evaluate the reactor performance quantitatively by comparing the energy consumption under different methods, the target delta was the same under these 3 methods in the reduction, and thus the total mole amount of oxygen removed is the same.

The energy input to the reactor Q_{reactor} can be devided into 5 parts:

$$Q_{\text{reactor}}=Q_{\text{Sense}}+Q_{\text{Red}}+Q_{\text{Oxid}}+Q_{\text{Loss}}+Q_{\text{O}_2} \tag{S1-1}$$

The reactor sensible heat is the required energy for heating the ceria from oxidation temperature (T_{Oxid}) to reduction temperature (T_{Red}) which is defined as:[1]

$$Q_{\text{Sense}}=(1-\varepsilon_{\text{s}})\int_{T_{\text{Oxid}}}^{T_{\text{Red}}} c_{\text{p,ceria}}\mathrm{d}T \tag{S1-2}$$

Energy required to drive the reduction reaction is defined as[1]:

$$Q_{\text{Red}}=0.5\int_{\delta_{\text{Oxid}}}^{\delta_{\text{red}}} \Delta h_{\text{O}_2,\text{ceria}}(\delta)\mathrm{d}\delta \tag{S1-3}$$

where δ_{Oxid} is the oxygen vacancy after complete oxidation listed in Table S4-2, the

The energy required to heat the CO_2 during oxidation is defined as[1]:

$$Q_{\text{Oxid}}=\left(1-\varepsilon_{\text{g}}\right)N_{\text{CO}_2}\int_{T_0}^{T_{\text{Oxid}}} c_{p,\text{CO}_2}\mathrm{d}T-0.5\int_{\delta_{\text{Red}}}^{\delta_{\text{Oxid}}} \Delta h_{\text{O}_2,\text{ceria}}(\delta)\mathrm{d}\delta \tag{S1-4}$$

Here, we consider the exothermic oxidation of the reactants.
The total energy in produced fuel is defined as:

$$Q_{\text{Fuel}}=N_{\text{CO}}\text{HHV}_{\text{CO}}=2N_{\text{O}_2}\text{HHV}_{\text{CO}} \tag{S1-5}$$

The n_{CO} is the total amount of CO produced in the oxidation step and the HHV_{CO} is the heating value of the CO. The molar amount of oxygen removed (N_{O_2}) is defined as:

$$N_{\text{O}_2}=(\delta_{\text{red}}-\delta_{\text{Oxid}})/2 \tag{S1-6}$$

The amount of heat loss due to heat conduction, heat convection and heat radiation is defined as:[2]

$$Q_{\mathrm{Loss}}=F_{\mathrm{Loss}}Q_{\mathrm{Sense}} \tag{S1-7}$$

The total mole of inert gas is defined based on a ideal mixture model:[3]

$$N_{\mathrm{N_2}}=0.5\int_{\delta_{\mathrm{Oxid}}}^{\delta_{\mathrm{Red}}}\frac{P_{\mathrm{Reactor}}-P_{\mathrm{O_2}}(T_{\mathrm{Red}},\delta)}{p_{\mathrm{O_2}}(T_{\mathrm{Red}},\delta)}\mathrm{d}\delta \tag{S1-8}$$

Where P_{Reactor} is the operation pressure of the thermochemical reactor, P_{O2} is the oxygen partial pressure in the reduction. Note that the P_{reactor} was equal to the ambient pressure (p_0 = 1 atm) in SG method and SG & EOP, while it was set as p_{VP} in SG + VP method.

The energy for oxygen removal varies in different oxygen removal methods:

$$Q_{\mathrm{O_2}} = Q_{\mathrm{SG}}+Q_{\mathrm{VP}}+Q_{\mathrm{EOP}} \tag{S1-9}$$

Where the $Q_{\mathrm{O_2}}$ is the energy for oxygen removal, Q_{SG} is the thermal energy used for heating the inert gas, Q_{VP} is the electric energy for driving the VP in oxygen removing, Q_{EOP} is the electric energy for driving the EOP for in situ oxygen removal. Note that $Q_{\mathrm{O_2}} = Q_{\mathrm{SG}}$ in the SG method, $Q_{\mathrm{O_2}} = Q_{\mathrm{SG}} + Q_{\mathrm{VP}}$ and in the SG + VP method, $Q_{\mathrm{O_2}} = Q_{\mathrm{SG}} + Q_{\mathrm{EOP}}$ and in the SG + EOP method, and $Q_{\mathrm{O_2}} = Q_{\mathrm{EOP}}$ and in the EOP method.

The thermal energy for heating the sweep gas is defined as:[3]

$$Q_{\mathrm{SG}}=N_{\mathrm{N_2}}\left(h_{\mathrm{N_2}}(T_{\mathrm{Red}})-h_{\mathrm{N_2}}(T_0)\right)+N_{\mathrm{O_2}}\left(h_{\mathrm{O_2}}(T_{\mathrm{Red}})-h_{\mathrm{O_2}}(T_0)\right) \tag{S1-10}$$

As the pump was driven by the electricity for oxygen removing in the SG & VP method, and Q_{VP} can be defined as[1]:

$$Q_{VP}=\left(N_{N_2}+N_{O_2}\right)RT_0\ln\left(\frac{p_0}{p_{VP}}\right)/\left(\eta_{ETP}\left(p_{VP}\right)\right) \quad \text{(S1-11)}$$

where R is the gas constant. The electricity to pump efficiency (η_{ETP}) depending on the p_{VP} which is defined as:[2]

$$\eta_{ETP}=a_0+a_1\lg\left(\frac{p_{VP}}{p_0}\right)+a_2\lg\left(\frac{p_{VP}}{p_0}\right)^2+a_3\lg\left(\frac{p_{VP}}{p_0}\right)^3+a_4\lg\left(\frac{p_{VP}}{p_0}\right)^4 \quad \text{(S1-12)}$$

the coefficient can be seen in Table S1-1. Note that the Q_{pump} = 0 under both SG and SG & EOP method, while the Q_{EOP} = 0 in both SG and SG & VP method.

Table S1-1 Coefficient of the electricity to pump efficiency

Coefficient	Value
a_0	0.30557
a_1	-0.17808
a_2	-0.15514
a_3	-0.03173
a_4	-0.00203

As the zero dimensional is independent of time, and the total oxygen removed is decided based on the P_{O2} and $T_{red,}$ the accumulated charge over the reduction (I_{EOP}) is thus defined as:

$$I_{EOP}=\frac{4FN_{O_2}}{A_{EOP}} \quad \text{(S1-13)}$$

The energy for the EOP is determined by the operation potential of EOP (V_{EOP}, V) and I_{EOP}:[4]

$$Q_{EOP}=V_{EOP}I_{EOP}A_{EOP} \quad \text{(S1-14)}$$

The operation potential of ideal EOP consisted of the equilibrium potential (E_{eq}), the

activation overpotentials (η_{act}), and the ohmic overpotential (η_{ohmic}):[5]

$$V_{EOP}=E_{eq}+\eta_{act,an}+|\eta_{act,ca}|+\eta_{ohmic} \quad \text{(S1-15)}$$

While for mass transfer limited EOP in which the oxygen diffusion limited the oxygen removal capability, the operation potential consists of concentration overpotential (η_{conc}) which can be defined as:[6]

$$V_{EOP}=E_{eq}+\eta_{act,an}+|\eta_{act,ca}|+\eta_{conc,an}+\eta_{conc,ca}+\eta_{ohmic} \quad \text{(S1-16)}$$

Based on the Nernst Equation, E_{eq} is defined as[4]:

$$E_{eq}=\frac{RT_{EOP}}{4F}\ln\left(\frac{P_0}{P_{O_2}}\right) \quad \text{(S1-17)}$$

where F is the Faraday's constant.
The relationship between the electrode activation overpotential and the current density can be expressed by the Butler-Volmer equation:[4]

$$I_{EOP}=\gamma_{O_2}\exp\left(-\frac{E_{act}}{RT_{EOP}}\right)\frac{RT_{EOP}}{F}p_{O_2}^{0.5}\left[\exp\left(\frac{2F\eta_{act}}{RT_{EOP}}\right)-\exp\left(\frac{-2F\eta_{act}}{RT_{EOP}}\right)\right] \quad \text{(S1-18)}$$

Where γ_{O_2} is the pre-exponential factor and E_{act} is the activation energy, the η_i is the activation overpotential (i = an, ca). For the electrolyte-based oxide cell of the EOP, the T_{EOP} ranged between 900 - 1100°C during the thermochemical cycle for the safe operation and to maintain the electrochemical performance.

The η_{conc} of the EOP is defined as:[6]

$$\eta_{conc}=\frac{RT_{EOP}}{2F}\ln\left[\left(1+\left(\frac{RT_{EOP}}{D_{O_2}^{eff}P_{O_2}^{0}}\frac{I_{EOP}}{4F}L_e\right)\right)^{0.5}\right] \quad \text{(S1-19)}$$

Where $D_{O_2}^{eff}$ is the effective oxygen diffusion coefficient,[7,8] $P_{O_2}^{0}$ is the initial oxygen partial pressure of the electrode, the subscript e indicate the electrode, L is the thickness of the component of EOP/ceria, for the cathode, $L_e = L_{ca}+L_{ceria}$. For this case, 1 mole

ceria is assumed with a 0.85 porosity which is same as the ceria fabricated in Section S7 and its shape is a cylinder in 0.06 m diameter.

The η_{ohmic} of the EOP is defined as:[9]

$$\eta_{\text{ohmic}} = 2.99 \times 10^{-5} I_{\text{EOP}} L_{\text{EOP}} \exp\left(\frac{10300}{T_{\text{EOP}}}\right) \tag{S1-20}$$

In this zero-dimension model, the ceria was directly heated by the solar energy, thus the solar-to-fuel efficiency (η_{STF}) of this zero-dimension model is defined as:

$$\eta_{\text{STF}} = \frac{Q_{\text{fuel}}}{Q_{\text{reactor}}} \times 100\% \tag{S1-21}$$

The energy constituent is used for analyzing different parts of energy consumption in the thermochemical reaction which is defined as:

$$f_{Q_i} = \frac{Q_i}{Q_{\text{Reactor}}} \tag{S1-22}$$

Where the subscript *i* indicate the Loss, Oxid, Fuel, O_2, and Sense.

The molar oxygen removal energy can be defined as:

$$q_{O_2} = \frac{Q_{O_2}}{M_{\text{ceria}}} \tag{S1-23}$$

The operation parameters for the baseline case are listed in Table S1-2.

Table S1-2 Baseline parameters used in the reference case

Parameter	Value	Unit
T_{Red}	1773.15	K
T_{Oxid}	1373.15	K
$P_{reactor}$	1(SG), 0.01(SG + VP, SG + EOP)	atm
δ_{Oxid}	0.001	—
F_{loss}	0.2	—
ε_s[10]	0.5	—
ε_g[10]	0.9	—
γ_{O2}[3]	1.344×10^{10}	$J \cdot mol^{-1}$
E_{act}[3]	1.0×10^{5}	$J \cdot mol^{-1}$
A_{EOP}	2.826×10^{-3}	m^2

Table S1-3 Operation parameters of the zero-dimension model

Parameters	Correlation
Heat capacity of ceria[12]	$c_{p,ceria}=-2.187\cdot10^{-5}T^2+4.634\cdot10^{-2}T+51.6120$
	$c_{p,ceria}=76.4654$ for $T>1100$ K
Heat capacity of CO_2[13] ($kJ\cdot mol^{-1}\cdot K^{-1}$)	$c_{p,CO_2}=24.9974+5.519\cdot10^{-2}\cdot T-3.3369\cdot10^{-5}\cdot T^2+7.948\cdot10^{-9}\cdot T^3-\frac{136638}{T^2}$ for $T<1200$ K
	$c_{p,CO_2}=58.1663+2.72\cdot10^{-3}\cdot T-4.9223\cdot10^{-7}\cdot T^2+3.8844\cdot10^{-11}\cdot T^3-\frac{6447293}{T^2}$ for $T>1200$ K
Reduction enthalpy[14] ($kJ\cdot mol^{-1}$)	$\Delta h_{O_2,ceria}=-1220\cdot e^{\left(-\left(\frac{\delta+0.1085}{0.2834}\right)^2\right)}-665.5\cdot e^{\left(-\left(\frac{\delta-0.06776}{0.07495}\right)^2\right)}-94.55\cdot e^{\left(-\left(\frac{\delta-0.1224}{0.08238}\right)^2\right)}+813.8\cdot e^{\left(-\left(\frac{\delta-0.06796}{0.08318}\right)^2\right)}-669\cdot e^{\left(-\left(\frac{\delta-0.3183}{0.1783}\right)^2\right)}$
Nitrogen (N_2) enthalpy[13] ($kJ\cdot mol^{-1}$)	$h_{N_2}=2.899\cdot10^{-2}\cdot T+9.27\cdot10^{-7}\cdot T^2-3.216\cdot10^{-9}\cdot T^3+4.159\cdot10^{-16}\cdot T^4-\frac{0.117}{T}-8.672$ for $T<500$ K
	$h_{N_2}=1.95\cdot10^{-2}T+9.943\cdot10^{-6}T^2-2.866\cdot10^{-9}T^3+3.424\cdot10^{-17}T^4-\frac{527.6}{T}-4.935$ for $T>500$ K

S2.2 Model results

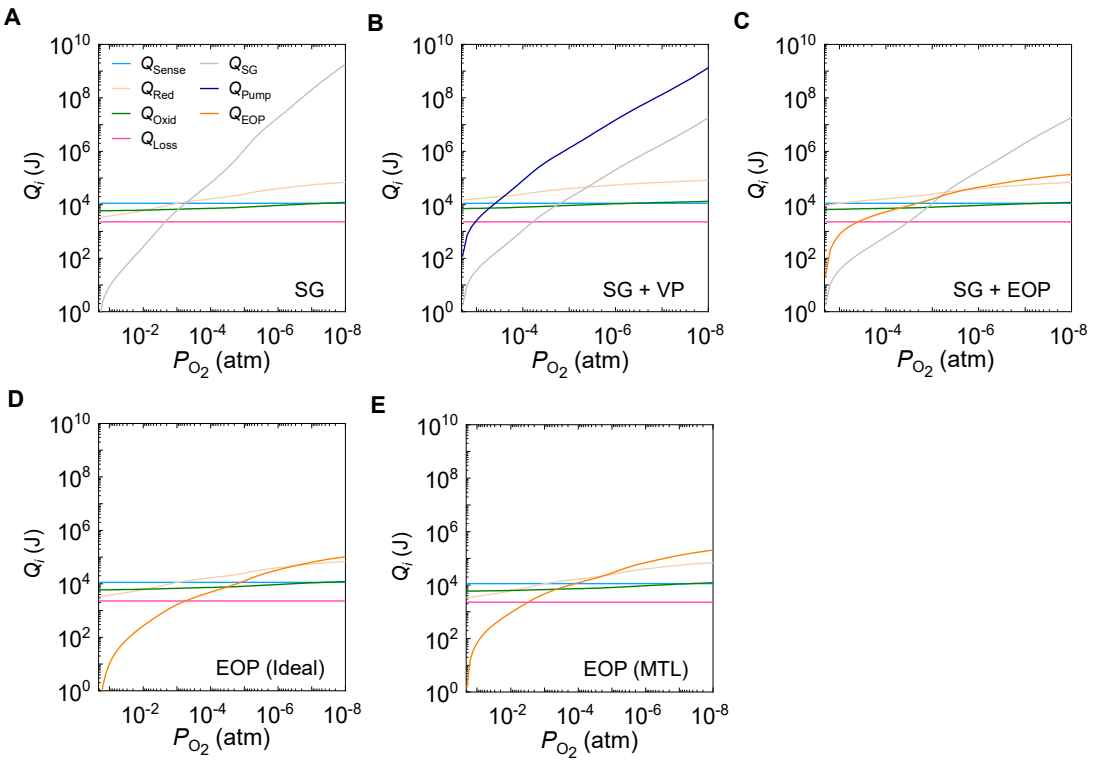

Figure S2-1. Energy input to the reactor under different oxygen removal methods as a function of P_{O_2}, (A) SG, (B) SG + VP, (C) SG + EOP, (D) EOP (Ideal), and (E) EOP (MTL).

Figure S2-1 presents the dependence of energy inputs as a function of oxygen partial pressure under different oxygen-removal strategies. Thermal terms (sensible heating, reduction and oxidation enthalpies, and losses) remain nearly constant, while auxiliary penalties rise sharply at low P_{O_2}. In SG, sweep-gas heating dominates; in SG + VP, pumping work increases steeply despite reduced sweep demand; in SG + EOP method, electrochemical work grows more gradually, offering higher efficiency; and in EOP method, the ideal configuration requires the least energy, whereas mass transfer limitation raises Q_{EOP}. These results explain the trend in Fig. 1E which shows η_{STF} increases with decreasing P_{O_2}, reaches an optimum, then declines as auxiliary penalties

dominate. For example, 17.96% in SG at 1.0×10^{-3} atm, improving to 21.07% with SG + VP at 5.01×10^{-4} atm as shown in Figure 1E.

A clear comparison can be made by examining the energy constituents of different oxygen-removal methods at their $\eta_{STF,\,max}$, which highlights how auxiliary penalties are distributed among the various schemes and sets the basis for the subsequent analysis.

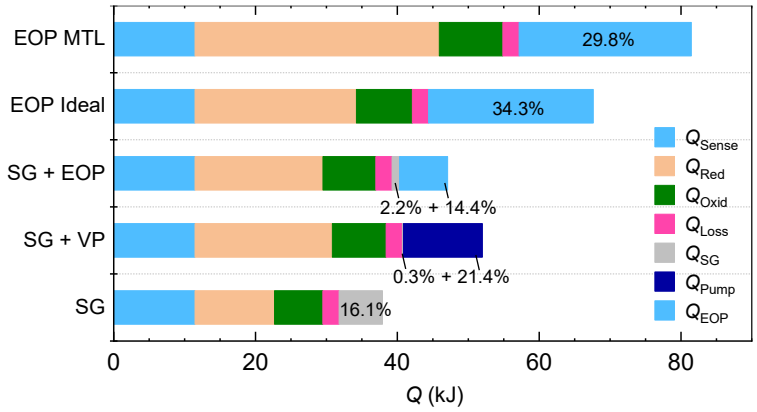

Figure S2-1. Energy constituent of different oxygen removal methods at $\eta_{STF,\,max}$.

For SG method, the thermal energy for heating the gas is non-negligible (Q_{SG} = 16.1%). For SG+VP, vacuum pumping dominates the auxiliary load compared to the sweep gas (Q_{Pump} = 21.4%, Q_{SG} = 0.3%). For SG+EOP, the electrochemical work remains modest (Q_{EOP} = 14.4%, Q_{SG} = 2.2%), yielding the smallest auxiliary share among EOP methods. For EOP (both the ideal and MTL cases) methods, electrochemical removal constitutes a large fraction of the budget (34.3% for ideal case and 29.8% for MTL case), with mass-transfer limits shifting additional energy into thermal components.

Overall, at the $\eta_{STF,\,max}$ operating points, SG+EOP minimizes auxiliary energy while keeping thermal inputs moderate, providing the most balanced, and thus most energy efficient for oxygen removal.

S2 Design of the EOP clamping tool for integration with the thermochemical reactor

S2.1 EOP clamping tool

The EOP, composed of a solid electrolyte-based cell, was integrated with the thermochemical reactor for oxygen removal. Spring loading was designed to maintain the gas sealing capability of the EOP. Pt mesh (99.999 %, 45mm OD, Fixawell) was spring loaded at both the cathode and anode before sintering. Two symmetric mica rings (50mm outside diameter (OD) , 40 mm inside diameter (ID), 2 mm thickness, Fixawell) are located between the Pt mesh and the shield to maintain electrical insulation and gas sealing at high temperature by utilizing their thermal expansion.

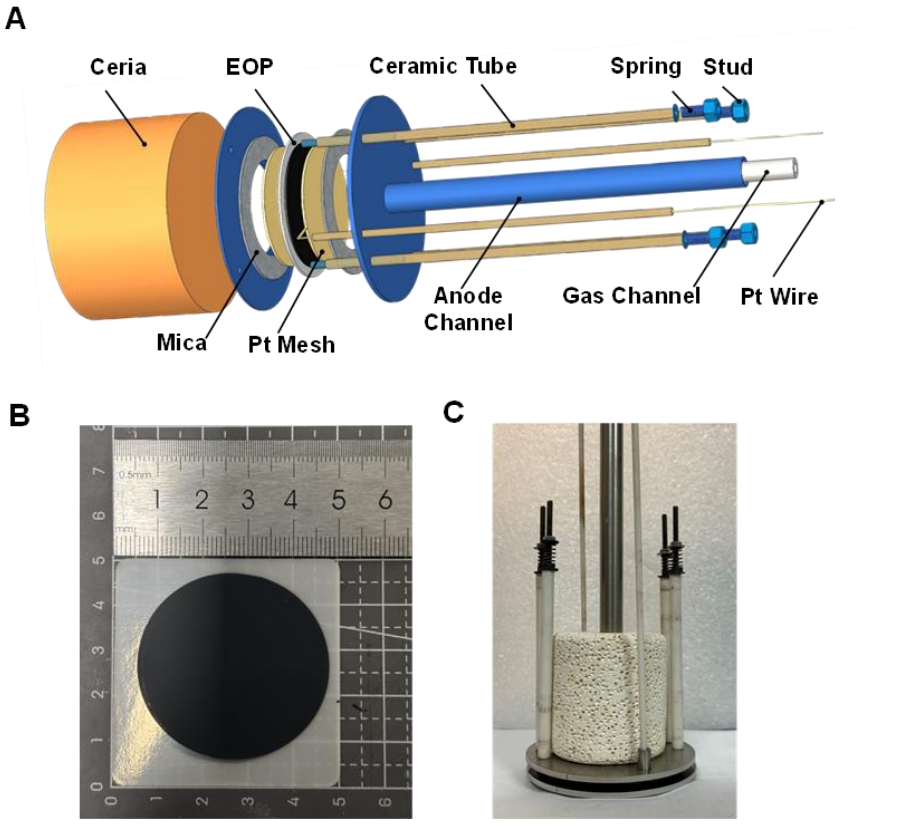

Fig. S2-1 (A) The structure of the designed EOP clamping tool with the ceria. (B) Fabricated EOP based on a commercial electrolyte. (C)Assembled spring loaded

arrangement in a front view.

The cathode and the anode shields (304 Stainless Steel) were assembled with metal threaded rods placed within long small diameter ceramic tubes (ZrO_2, 6 mm OD, 4mm ID, 100 mm length). Springs maintained at ambient temperature outside of the hot zone insured sealing of components during thermochemical reactions taking place at elevated temperatures. Al_2O_3-based cement (552T, Aremco) coated the joint area between the mica and the shield for improved sealing. The explosed view of the clamped setup (including the ceria) can be seen in Figure S1-1a, and the assembled EOP clamped setup can be seen in the Fig S1-1B. The fabricated EOP based on coating composite electrode slurry on a planar electrolyte (5 cm × 5cm, 100 μm thickness, Fuel Cell Materials) can be seen in Fig S1-1C. Both the cathode and anode consist of a single-layer LSM/YSZ composite, chosen for its overall mixed ionic ad electronic conductivity. The LSM fraction in the LSM-YSZ composite was $(La_{1-x}Sr_y)_{0.95}MnO_{3\pm\delta}$ with x=y=0.25, while the YSZ fraction in the electrode was 8 mol% Y_2O_3 (TZ8Y, Tosoh Corporation). Additionally, 10 wt% graphite powder (MAG-106, MTI Corporation) was used as the perforating agent. 95 wt% terpineol (T818820, Macklin) and 5 wt% ethyl-cellulose (E809013, Macklin) mixed with these three powders were ball milled for 6 hours into a slurry before applying 4 successive screen printed layers on the electrolyte to form an overall electrochemical active 5 - 9 μm thick layer. The cell was then sintered at 1373 K for 5 hours at a heating rate of 1 $K \cdot min^{-1}$ from 273 K to 873 K and at 2 $K \cdot min^{-1}$ from 873 K to 1373 K using the Muffle furnace (KSL-1750X, MTI).

S2.2 Solar-driven thermochemical reactor system

The overall EOP and thermochemical reactor was assembled prior to testing to check its gas sealing performance (see details in Section S2.3).

The main element of the system was the thermochemical reactor facing the HFSS central module. The thermochemical reactor is located on the 3D moving platform for

adjusting the relative distance between the focal plane of the HFSS central plane and the reactor. The volumetric flow rate of the gas was controlled by the MFCs (CS2000, Seven Star) before entering the reactor. The production gas was introduced for gas analysis before entering the exhaust hood. The DC supply (2280S-32-6, Keithley) drove the EOP in the SG + EOP method and the EOP method and all the data were recorded by the data logger (DMM6500, Keithley). The front view of the reactor can be seen in Fig. S2B and the back view in Fig. S2-2C. Note that the adjacent area between the ceramic tube and the back shield of the reactor, as well as the tool channel, were sealed by the Al_2O_3 adhesive (552T, Aremco), the white part on the shield, for over 24 hours for drying before initiating the thermochemical cycles.

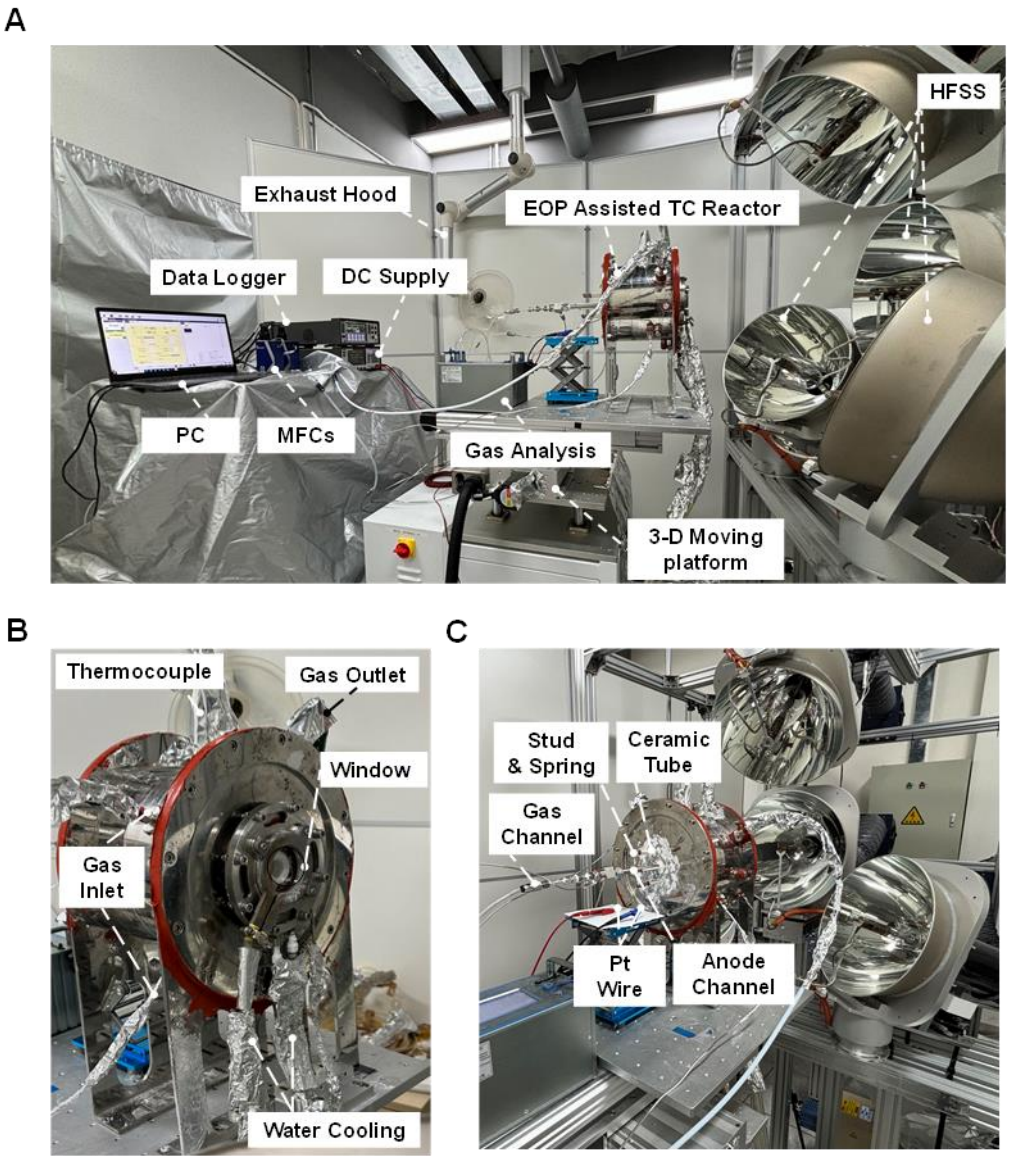

Fig. S2-2 Solar-driven thermochemical reactor system for carbon reduction assisted by EOP. (A) Demonstration of thermochemical system. (B) Front view of thermochemical reactor. Window water cooled, driven by water circulation through chiller. (C) Back view of thermochemical reactor.

In reduction, only the central module of the HFSS drives the thermochemical reaction, of which the heat flux distribution (characterized by the indirect method) can be seen in Figure S2-3.

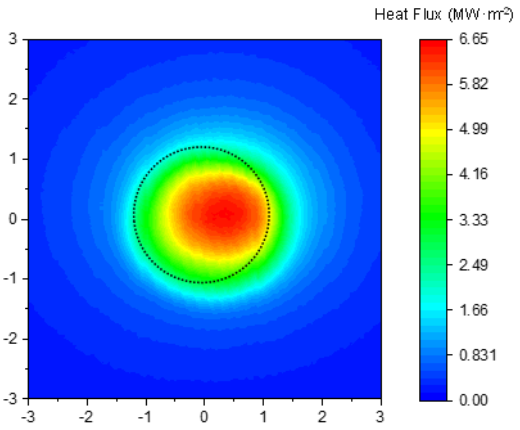

Figure S2-3. Heat flux distribution of the central module of the HFSS. The dashed circle represents the window of the thermochemical reactor.

S2.3 Sealing performance of EOP-assisted thermochemical reactor

Before the thermochemical performance was tested, the reactor gas sealing was first examined in both ambient temperature and high temperature (with HFSS turned on). In ambient temperature, a constant volumetric argon flow was introduced to the reactor controlled by the MFC. The gas flow rate from the outlet was measured by the MFCs in digital mode. The $\dot{v}_{Ar}$ ranged from 50 - 4000 sccm, the flow rate equal in the 3 methods. Note that the maximum $\dot{v}_{Ar}$ was 2000 sccm, so the $\dot{v}_{Ar}$ = 4000 was measured based on two MFCs with solo-direction values. There was no argon introduced to the anode and the anode channel was introduced to the MFC for measuring the gas flow rate to judge whether there existed a gas leakage. Each test duration for different $\dot{v}_{Ar}$ lasted 60 minutes, longer than a benchmark thermochemical cycle. The gas sealing performance of the reactor at ambient temperature can be seen in Figure S2-4A and S2-4B.

At high temperature, the active cooling method was not applied. The gas sealing testing procedure at high temperature was consistent with it at ambient temperature, except replacing argon by O_2 for surpassing the oxygen generation which may increase the

outlet gas flow rate. The gas sealing performance of the reactor at high temperature can be seen in Figure S2-4C and S2-4D.

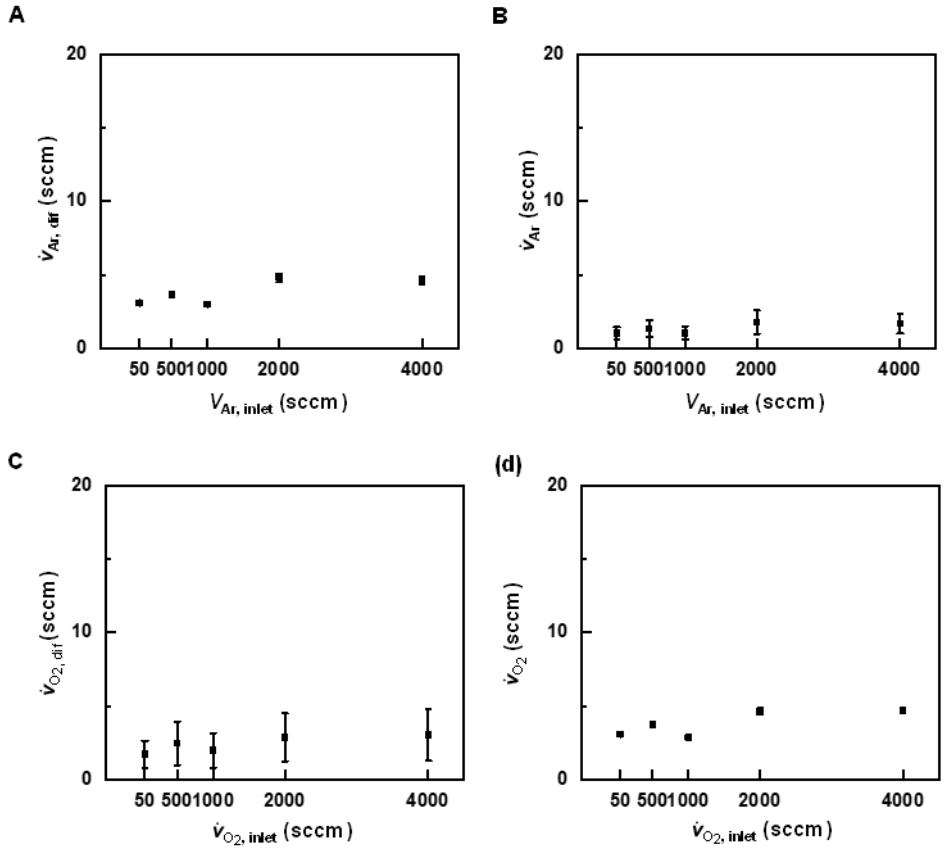

Fig S2-4. The gas sealing performance of reactor in both ambient and high temperature. At ambient temperature: (A) Argon flow rate difference ($\dot{v}_{A,\ dif}$, sccm) between the reactor inlet and outlet as a function of $\dot{v}_{Ar,\ inlet}$, (B) $\dot{v}_{Ar}$ at the outlet of the gas channel of the EOP as a function of $\dot{v}_{Ar,\ inlet}$. At high temperature: (C) $\dot{v}_{O_2,\ dif}$ between the inlet and outlet as a function of $\dot{v}_{O_2,\ inlet}$, (D) $\dot{v}_{O_2}$ at the outlet of the gas channel of the EOP clamping tool as a function of $\dot{v}_{O_2,\ inlet}$.

At room temperature, the $\dot{v}_{A,\ dif}$ between the inlet and the outlet did not exceed 5.3 ± 0.22 sccm and $\dot{v}_{Ar}$ at the outlet of the gas channel of the EOP was less than 2.4 ± 0.52 sccm which are less than 20 sccm. Since the MFC has a specified accuracy of ±1% of full scale (2000 sccm, i.e., 20 sccm), deviations below this threshold fall within

instrumental uncertainty and thus confirm the absence of measurable leakage. At high temperature, the $\dot{v}_{O_2,\,dif}$ and $\dot{v}_{O_2}$ at the outlet of the gas channel of the EOP were also less than 20 sccm. Hence, the reactor can maintain the gas sealing capability in both ambient and high temperature.

S3 Accuracy of gas analysis

The gas analysis based on the IR detector was able to conduct the continuity testing while gas chromatography (GC) could analyze the gas mixture but at the cost of longer time. The accuracy of the gas analysis was tested based on the GC and the procedure is illustrated in Figure S3-1A.

During thermochemical reactions, as the oxygen partial pressure ranged between 1.0×10^2 - 2.1×10^6 ppm and the p_{CO} ranged from 1.0×10^2 - 1.0×10^5 ppm. The results can be seen in Figure S3-1B and S3-1C.

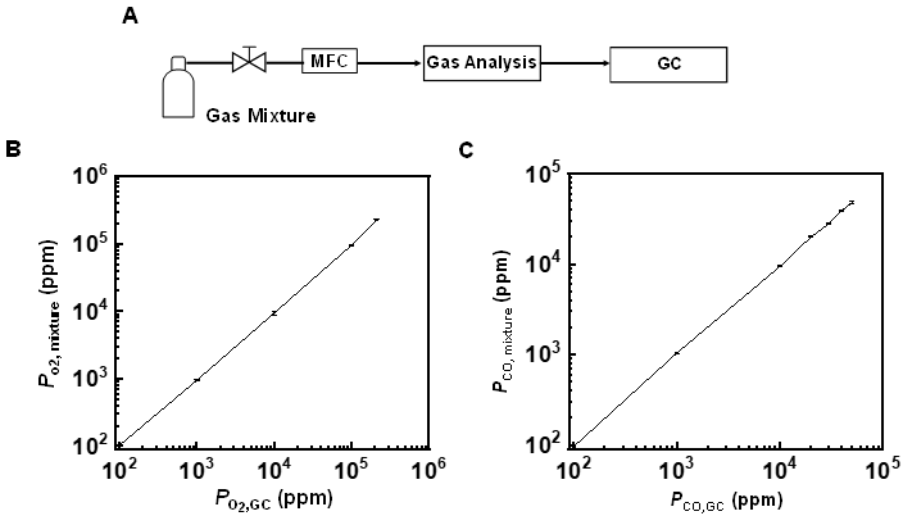

Fig S3-1. (A)Schematic operation of gas analysis based on the GC. (B) Measured error of P_{O_2} by the gas analysis as a function of $P_{O_2,GC}$ measured by GC. (C) Relative error of P_{CO} measured by gas analysis as a function of $P_{CO,GC}$.

The standard gas mixture controlled by the MFC (CS2000, Seven Star) was first introduced to the gas analysis (TY-6030P, Wuhan Zhiyu Tech.) based on the IR detector before introducing it to the GC (GC9790Plus, Fuli Instrument). The results showed that the maximum relative error based on the GC of P_{O_2} was 1.0 % (at $P_{O2,GC} = 1 \times 10^4$ ppm) and of P_{CO} was 5.6 % (at $P_{co,GC} = 1 \times 10^3$ ppm).

S4 Experimental setup of the 3 oxygen removal methods

Three methods were proposed for the investigation of the experiments in the reduction which are the Sweep Gas (SG) method, the EOP method, and SG + EOP method. Before the HFSS was turned on in the reduction, the inert gas (Ar) was introduced to the reactor for sweeping out the remaining oxygen until the P_{O_2} of the outlet gas was less than 1×10^{-4} atm to avoid the impact from the remaining gas on the ceria oxygen generation. When the reduction began, the HFSS was turned on and $\dot{v}_{Ar}$ was tuned to the required rate in the different oxygen removal methods, with the details of all the methods introduced in the following sub-sections. Reduction was followed by oxidation in which the fuel (CO) was produced from CO_2 by exposure to the reduced ceria.

S4.1 SG method

In the SG method, only argon was ultilized as the sweep gas for oxygen removal in the reduction reaction. The $\dot{v}_{Ar}$ varied from 500 to 4000 sccm in different cycles once the HFSS was turned on. When the oxidation started, the HFSS was turned off before shifting the argon to CO_2 at the constant volumetric flow rate ($\dot{v}_{CO_2}$) of 3000 sccm. The schematic of the SG method is shown in Fig S4-1.

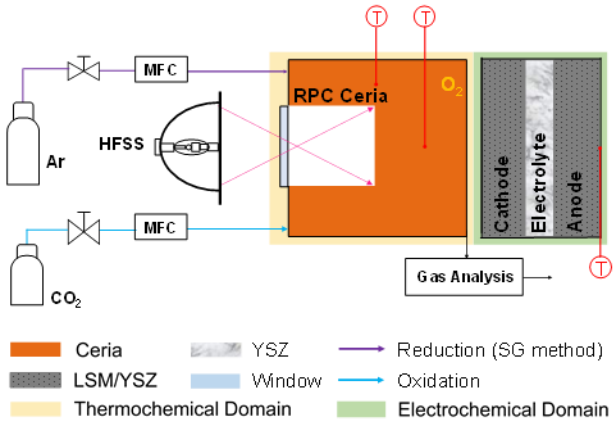

Figure S4-1. Schematic of EOP assisted thermochemical reactor for carbon dioxide

reduction system in the SG method. The purple solid arrow represents the inert gas which sweeps the ceria to reduce the P_{O_2} during reduction, the blue solid arrow represents CO_2 transport during oxidation which is reduced to CO by the ceria. The pink solid arrow represents the edge ray of the HFSS. The orange background represents the thermochemical domain, and the green background represents the electrochemical domain.

S4.2 EOP method

In EOP method, the EOP was driven by a DC supply for electrochemically pumping oxygen. While a minor $\dot{v}_{Ar}$ was introduced to measure the ceria P_{O_2} which represents the oxygen generation rate of ceria. Comparing the $\dot{v}_{Ar}$ used in the SG method, the $\dot{v}_{Ar}$ in this method was constant at 50 sccm. The V_{EOP} ranged from 0.5 V to 2.0 V during reduction only. In the oxidation reaction, $\dot{v}_{CO_2}$ was set as 2000 sccm. The schematic of the EOP method is shown in Figure S4-3.

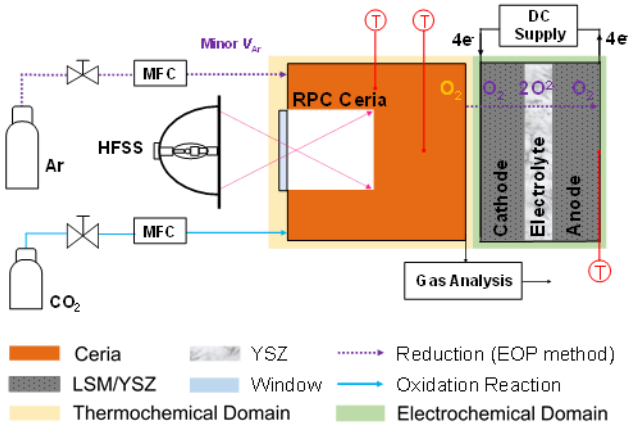

Figure S4-2. Schematic of EOP assisted thermochemical reactor for carbon dioxide reduction system in the EOP method. The purple dash-dot arrow represents the minor flow rate from the MFC, while it represents the oxygen pumping process in the EOP domain. The pink solid arrow represents the edge ray of the HFSS. The blue solid arrow represents the CO_2 transport that is reduced to CO upon exposure to reduced ceria. The orange background represents the thermochemical domain, and the green background represents the electrochemical domain.

The reduction duration was longer than that in SG + EOP method and the oxidation

step lasted 15 minutes to prevent the EOP from cracking due to rapid cooling.

S4.3 SG + EOP method

In the SG + EOP method, both EOP and argon were simultaneously used for oxygen removal. The argon flow not only reduced the P_{O_2} but also enhanced the oxygen transfer from ceria to the EOP, while the EOP removed the oxygen electrochemically. Note that $\dot{v}_{Ar}$ ranged from 500 sccm to 2000 sccm while the EOP V_{EOP} ranged from 0.5 V to 1.0 V. In the baseline case shown in Fig 2b, the $\dot{v}_{Ar}$ was set as 1000 sccm. The $\dot{v}_{CO_2}$ was 3000 sccm in the oxidation. Schematic of the SG + EOP method is shown in Figure S4-3.

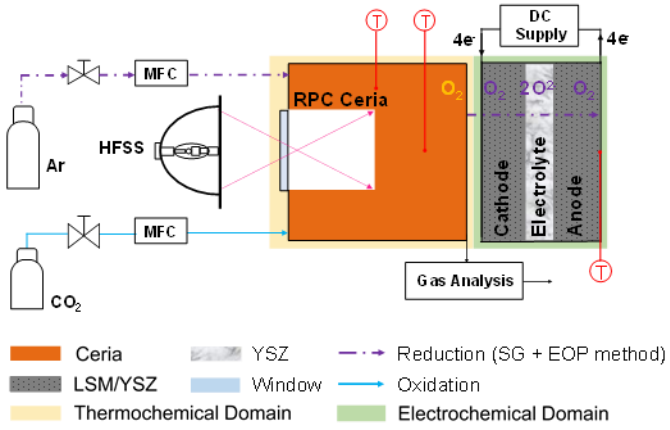

Figure S4-3. Schematic of EOP assisted thermochemical reactor for fuel production system in the SG + EOP method. The purple dashed arrow represents the argon flow rate controlled by the MFC, while it represents the oxygen pumping process in the EOP domain (O_2 reduced in the cathode into O^{2-} before migrating across the electrolyte and oxidized back to O_2 in the anode). The pink solid arrow represents the edge ray of the HFSS. The blue solid arrow represents the CO_2 transport which is reduced to CO by ceria. The orange background represents the thermochemical domain, and the green background represents the electrochemical domain.

S5 Optimization of the experiments

S5.1 Energy input and reaction time

The solar-to-fuel efficiency (η_{STF}) of the thermochemical cycle is defined as: [15]

$$\eta_{STF}=\frac{\Delta H_{CO}\int r_{CO}dt}{\int P_{solar}dt+E_{penalty}} \quad \text{(S5-1)}$$

Where the ΔH_{CO} is the molar heating value of the CO (ΔH_{CO} = 283 kJ·mol^{-1}), r_{CO} is the CO generation rate during the oxidation, P_{solar} is the solar radiative power input, and the $E_{penalty}$ is the energy consumption for oxygen separation in the reduction.

For VP, $E_{penalty}$ was defined as:

$$E_{penalty} = Q_{VP} = (N_{N_2}+N_{O_2})RT_0 \ln(\frac{p_0}{p_{VP}})/(\eta_{ETP}p_{VP}) \quad \text{(S5-2)}$$

While for EOP, which aimed at in situ oxygen removal driven by a DC supply defined as:

$$E_{penalty} = Q_{EOP}=\int V_{EOP}I_{EOP}A_{EOP}dt \quad \text{(S5-3)}$$

Where the I_{EOP} is the EOP current density in the reduction, A_{EOP} is the EOP electrode area.

Note that when both the EOP and VP were driven by the PV cell which supplies the direct currency, the solar energy for the EOP and VP can be defined as:

$$Q_{Solar,\ VP} = (N_{N_2}+N_{O_2})RT_0 \ln(\frac{p_0}{p_{VP}})/(\eta_{STE}\eta_{ETP}p_{VP}) \quad \text{(S5-4)}$$

$$Q_{\text{Solar, EOP}} = V_{\text{EOP}} I_{\text{EOP}} A_{\text{EOP}} / \eta_{\text{STE}} \quad \text{(S5-5)}$$

where the η_{STE} is the solar-to-electricity efficiency, η_{STE} = 23%.[4]

To simplify the analysis, based on mass conservation, the cumulative oxygen (mol) is doubled to estimate the production of carbon monoxide (mol), and the relationship between the η_{STF} and time (t) was determined according to Equation S5-1. In the typical operating conditions, the relationship between η_{STF} as a function of time was measured using the $\dot{v}_{\text{Ar}}$ at 2000 sccm, aiming to optimize the reduction duration. The baseline case result can be seen in Fig. S5-1A.

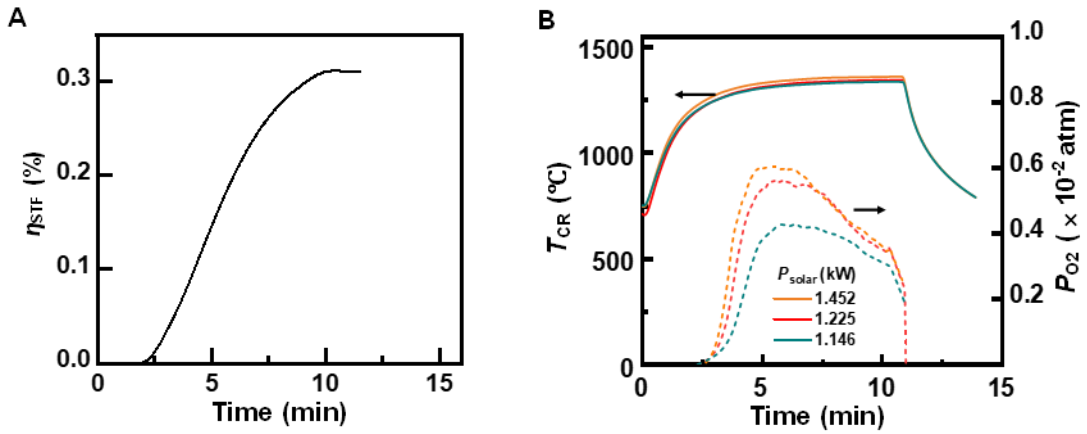

Fig S5-1 (A) η_{STF} in SG method at $\dot{v}_{\text{Ar}}$ = 2000 sccm as a function of time. (B) Reactor performance of the thermochemical reactor. Solid Line: T_{CR}, Dashed Line: P_{O_2}. Colors represent P_{solar}: orange represents 1.452 kW, red - 1.225 kW, green - 1.146 kW.

The results showed that the maximum η_{STF} was obtained at around 630 s. The optimized reduction duration for both the PSG method and the SGAE method was chosen as 630 s to maximize η_{STF} and evaluate the reactor performance under the same framework.

In the thermochemical reaction, the concentrated solar rays travel through the transparent window and are absorbed by the ceria to drive the thermochemical reaction. However, the edge ray of the solar energy incident on the water cooling region between

the window and the ceria (see ***Graphic Abstract*** for details) would reduce the total energy received by the ceria, depending on the relative distance of the reactor and the focal plane of the HFSS central module. As this relative distance ranged from 10 mm to 30 mm to avoid the focal point locating on the window or outside the reactor, the integrated solar irradiation ranged from 1.146 kW_{th} to 1.452 kW_{th}. The η_{STF} obtained under different P_{solar} conditions can be seen in Table S5-1 and the thermochemical performance can be seen in Fig S5-1B. The highest η_{STF} was obtained at P_{solar} = 1.225 kW. Thus, the optimized P_{solar} was chosen as 1.225 kW.

Table S5-1 Relation between the η_{STF} and P_{solar}

P_{solar} (kW_{th})	1.146	1.225	1.452
η_{STF} (%)	0.278	0.336	0.301

In the reduction, the heat flux distribution of the central module at different planes can be seen in Figure S5-2. The heat flux distribution of P_{solar} = 1.225 kW_{th} can be seen in Figure S2-3.

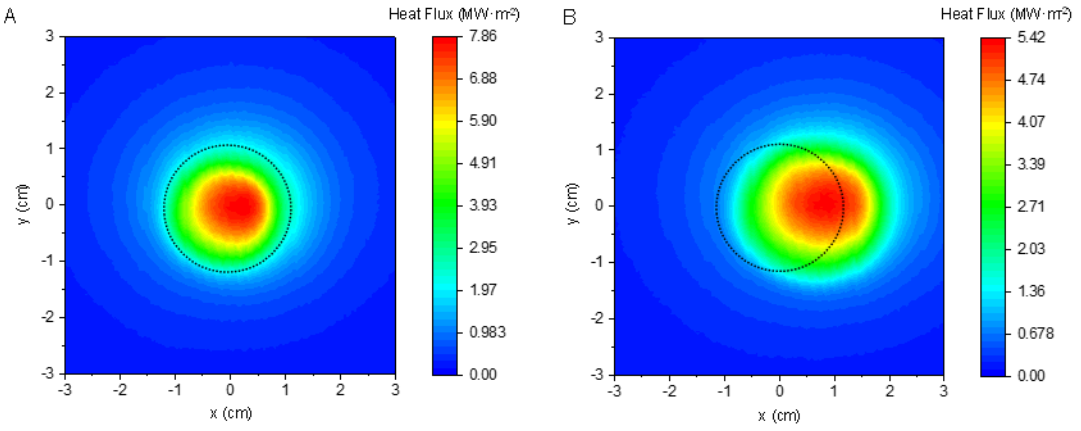

Figure S5-2. The Heat flux distribution of the central module of the HFSS at different planes. The dash circle represents the window of the thermochemical reactor. (A) P_{solar} = 1.452 kW_{th}, (B) P_{solar} = 1.146 kW_{th}.

S5.2 Temperature variations

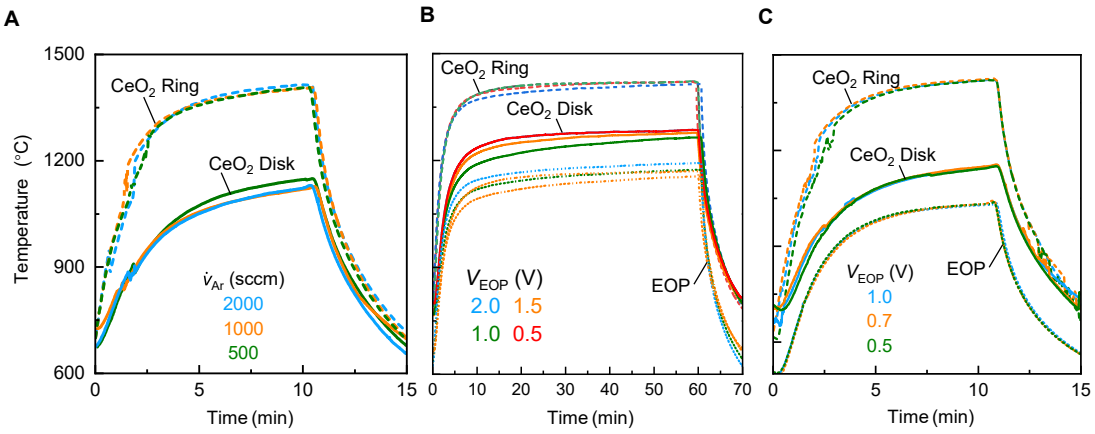

Figure S5-3. Temperatures as functions of time in different oxygen removal methods (A) SG, (B) SG + VP, and (C) SG + EOP.

Figure S5-3 compares the transient temperature profiles of the ceria ring (T_{CR}) and ceria disk (T_{CD}) under the three oxygen-removal strategies. In the SG method (Fig. S5-3A), both T_{CR} and T_{CD} rise steadily during the initial 5 min and reach their maxima near 10 min. Increasing the sweep gas flow rate from 500 to 2000 sccm causes the T_{CD} to decrease by about 24.1°C (from 1148.2°C to 1124.1°C) at 10 min, whereas the maximum T_{CR} shows only minor variations of less than 4.2°C, indicating that the disk is more sensitive to enhanced convective heat removal.

In the SG+EOP method as shown in Figure S5-3B, V_{EOP} further influences the temperature response. With V_{EOP} = 0.5V, both T_{CR} and T_{CD} exhibit a faster initial rise compared to SG, stabilizing at elevated levels before 10 min and maintaining higher plateaus throughout reduction. The EOP current increases oxygen removal, which reduces local oxygen partial pressure and facilitates higher heat absorption in the porous ceria structure. For the EOP method as shown in Figure S5-3C, the trends are similar, but without the convective effect of large sweep flows. T_{CD} is slightly higher than that in SG method at the same time, reflecting reduced heat loss from sweeping gas. The T_{CR}, however, remains relatively constant, showing small variations regardless of

increased V_{EOP}, further confirming that the ring experiences more uniform heating while the disk is more sensitive to mass transfer and heat removal.

S6 Oxygen removal contribution

In both the SG +EOP method and the EOP method, the EOP and the argon flow simultaneously remove oxygen in the reduction, while in the SG method, only the inert gas (argon) sweeps the ceria to reduce the oxygen partial pressure.

The total molar oxygen removed in the reduction step is defined as:

$$R_{O_2,\,Total} = R_{O_2,EOP} + R_{O_2,\,SG} \tag{S6-1}$$

where $R_{O_2,\,EOP}$ is the molar oxygen removed by EOP via the electrochemical reaction, and $R_{O_2,\,SG}$ is the molar oxygen removed by the inert gas.

$R_{O_2,\,EOP}$ is defined according to Faraday's Law as:

$$R_{O_2,EOP} = \frac{\int I_{EOP} A_{EOP} dt}{n\mathrm{F}} \tag{S6-2}$$

where $n = 4$ in oxygen removal.

$R_{O_2,\,SG}$ is defined as:

$$R_{O_2,\,SG} = \frac{\int P_{O_2} V_{Ar} dt}{V_{mol}} \tag{S6-3}$$

where V_{mol} is the molar volume of the ideal gas.

The EOP contribution in oxygen removal is defined as:

$$f_{O_2,EOP} = \frac{R_{O_2,EOP}}{R_{O_2,\,Total}} \times 100\% \tag{S6-4}$$

The molar oxygen removal rate for the SG method is defined as:

$$\dot{M}_{O_2} = \frac{P_{O_2} V_{Ar}}{V_{mol} M_{ceria}} \quad \text{(S6-5)}$$

where M_{ceria} is the number of moles of ceria.

While for both the EOP and SG + EOP method, $\dot{M}_{O_2}$ is defined as:

$$\dot{M}_{O_2} = \frac{P_{O_2} V_{Ar}}{V_{mol} M_{ceria}} + \frac{I_{EOP} A_{EOP}}{n \mathrm{F} M_{ceria}} \quad \text{(S6-6)}$$

S7 Details of ceria fabrication

The RPC (Reticulated Porous Ceramic) ceria was fabricated via coating a ceria slurry on the designed polyurethane matrix (see Fig S7-1A and Fig S7-1B).

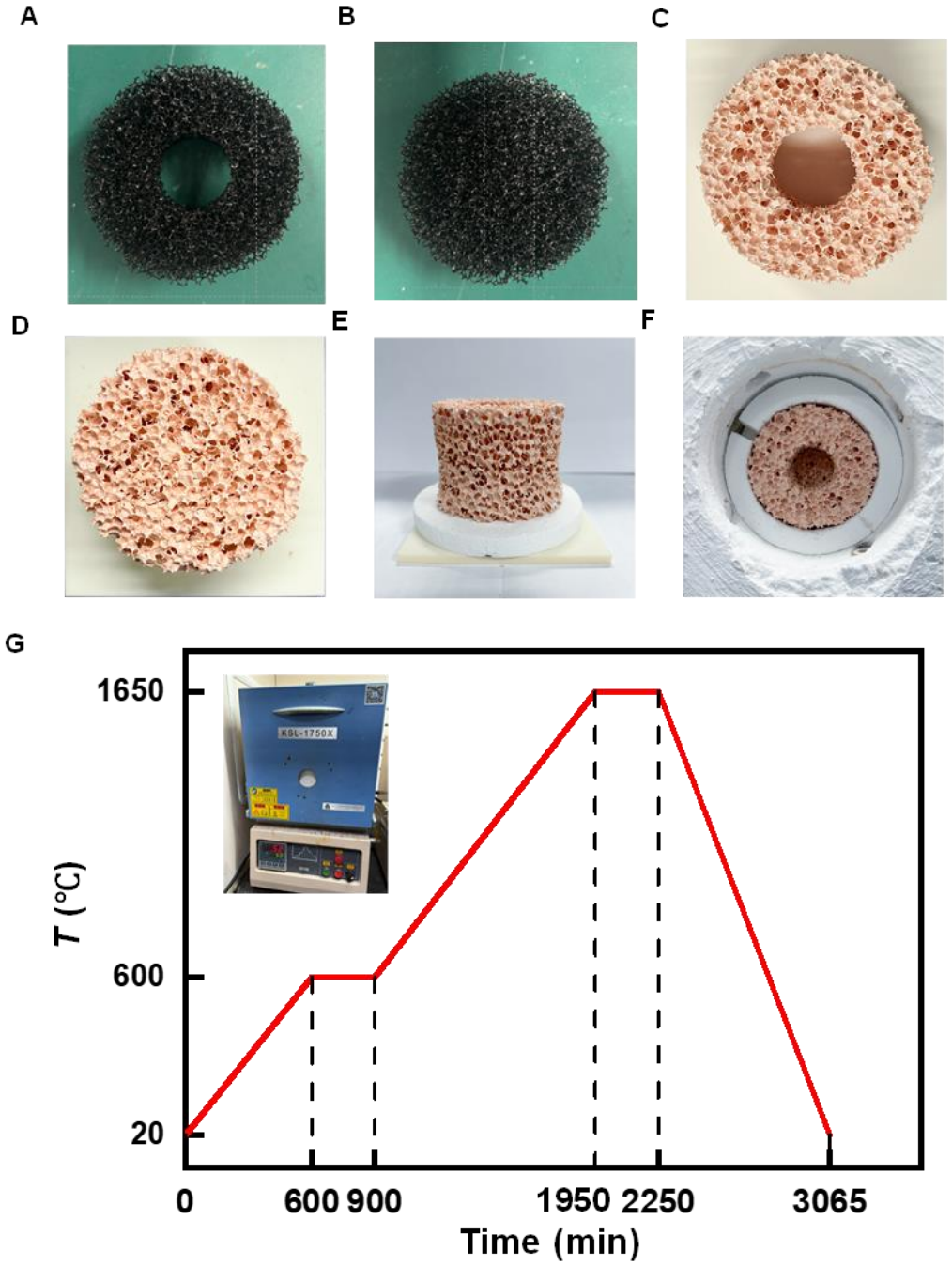

Fig S7-1. RPC Ceria fabricated for the solar thermochemical reactor. A set of

polyurethane matrix includes a (A) ring (Outside Diameter, OD: 90 mm. Inside Diameter, ID: 40 mm. 30 mm thickness) and a (B) disk (90 mm OD. 30 mm thickness). A set of ceria after sintering consists of (C) disk (25 mm thickness, 60 mm OD) and (D) one ring (25mm thickness, 25 mm ID, 60 mm OD). (E) Pristine ceria set and (F) ceria set assembled within the insulation from a front view before initiation of thermochemical reactions. Ceria set mass: 112.2 ± 0.74 g. (G) Sintering treatment process. Inset: sintering furnace.

The starting powder for the ceria slurry was a mixture of coarse ceria (Aladdin, 99.99%, 100-500 μm) and fine ceria (Aladdin, 99.999%, < 50 nm) combined in a 7: 3 mass ratio. acrylate ammenium (Aladdin, $(C_3H_7O_2N)_m$, 40 % in water) was added as a dispersant and carboxymethyl cellulose (Mreda, 800 - 1200 $Pa \cdot s^{-1}$) was added as the binder. Then the dispersant and binder, as well as the powder, were ball-milled for 12 h using YSZ (Yttria-stabilized ZrO_2) grinding media. The ceria slurry was then coated on the polyurethane matrix before being dried in air for 2 hours. Note that six repetitions of this coating-dried step were applied before the coating samples were sintered under stagnant air to gently remove the polyurethane matrix and carbon pore-former. The sintering treatment was selected based on the thermal decomposition behavior of the organic components as guided by thermogravimetric analysis. The maximum sintering temperature was higher than the benchmark reduction temperature for stable operation. The sintered RPC ceria ring and ceria disk can be seen in Fig S7-1E and Fig S7-1F. Details of the sintering treatment can be seen in Fig S7-1G.

S8 Microstructure of pristine ceria and cycled ceria

The average grain size of the pristine ceria was analyzed based on the SEM results in different scale bars ranging from 10 μm to 200 μm on both the surface and the fracture plane. More SEM images of pristine ceria can be seen in Fig S8-1, and of cycled ceria can be seen in Fig S8-2. The grain boundaries are highlighted in red borders processed in softeware *ImageJ*.

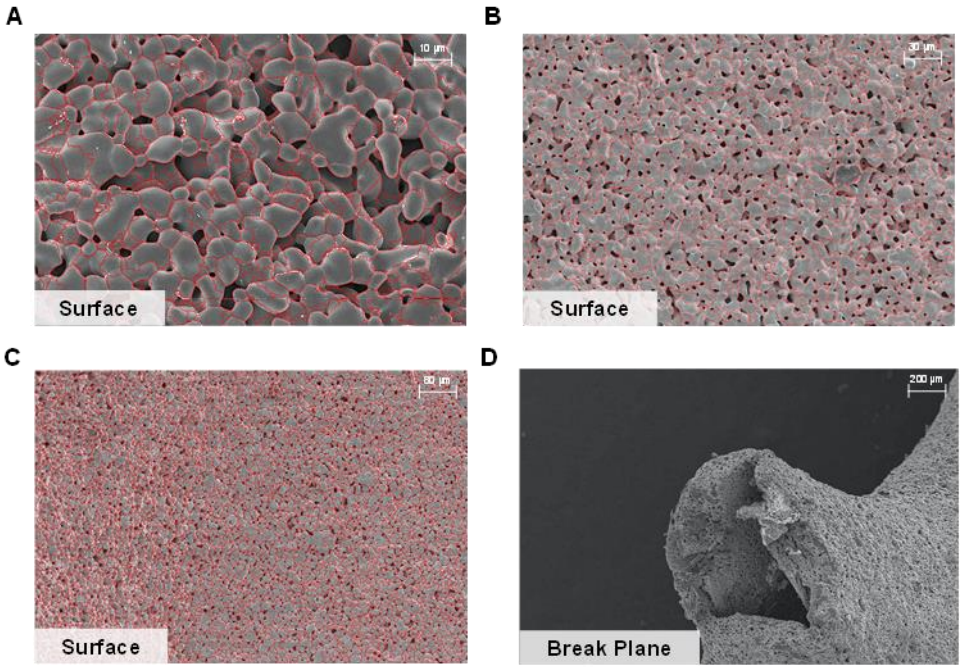

Fig S8-1. SEM image of the pristine ceria. Ceria surface in different scales are shown in: (a) scale bar: 10 μm.(b) scale bar: 50 μm. (c) scale bar: 80 μm. Ceria fracture plane is shown in (d) scale bar: 200 μm.

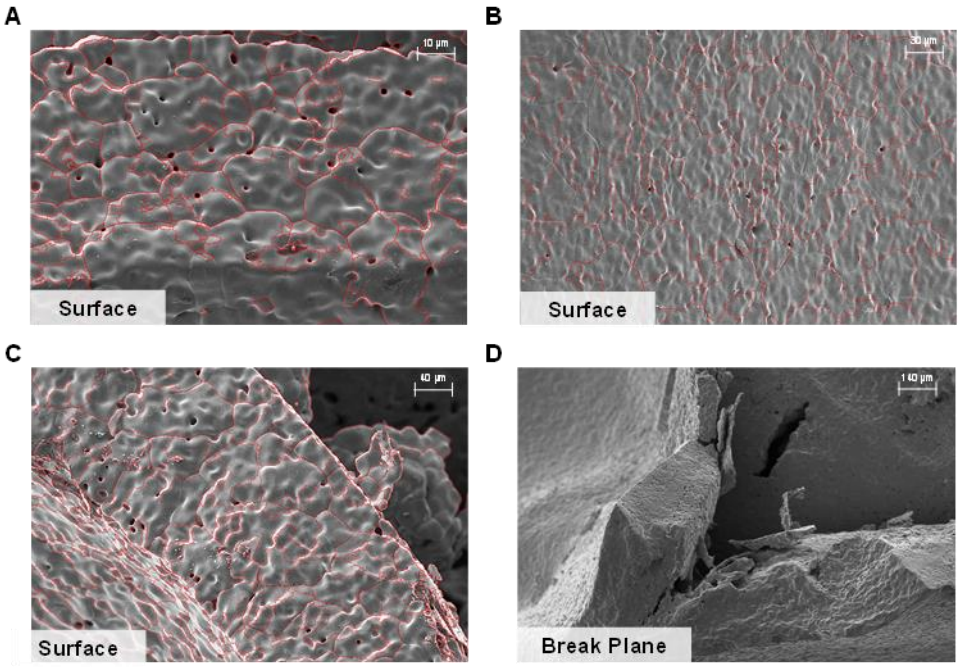

Fig S8-2. SEM image of cycled ceria. Ceria surface in different scale are shown in: (a) scale bar: 10 µm.(b) scale bar: 30 µm. (c) scale bar: 40 µm. Ceria fracture plane is shown in (d) scale bar: 140 µm.

There existed Tiny regions were found on the ceria surface after oxidation as shown in Figure 3D (right inset, a small region on the surface of the ceria) in dark blue. For identifying the cause, a new set of pristine ceria was tested in the thermochemical cycle in the SG method, while the inert gas was still introduced to the ceria in the oxidation step, which meant the oxygen vacancies remained in the ceria. After turning off the HFSS and cooling to the ambient temperature, the condition of the ceria is shown in Fig S8-3.

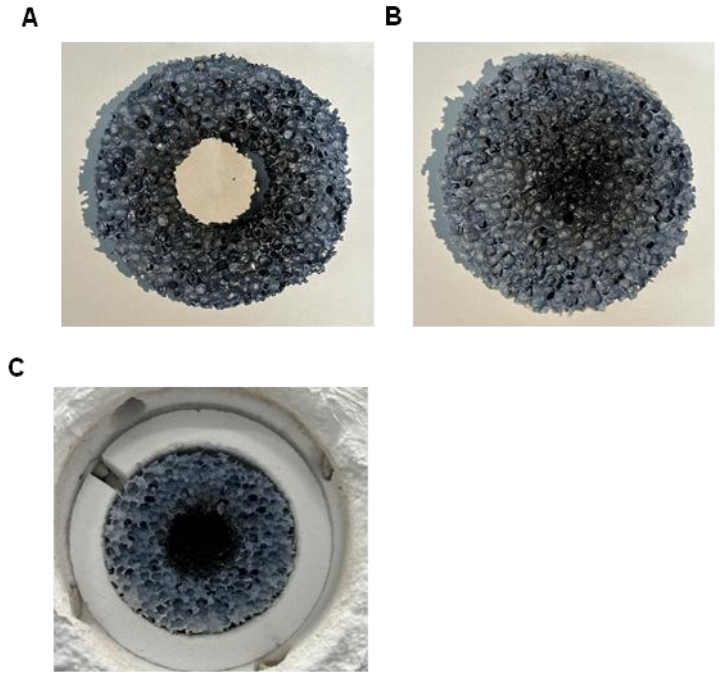

Fig S8-3. (A) ceria ring with oxygen vacancies, (B) ceria disk with oxygen vacancies, (C) ceria set in the reactor after cooling to the ambient temperature.

The difference in the ceria color between ceria without and ceria with oxygen vacancies proved that the dark blue region in ceria could be attributed to insufficient oxidation.

S9. Economic Assessment of the average fuel cost under different methods

S9.1 Introduction of economic model

The following assumptions are made for the techno-economic model: (i) $\eta_{optical}$ is defined by the heliostat distribution and optical parameters specific to each location and the η_{STH} is calculated hourly based on site-specific DNI and a fixed reduction temperature of 1500 °C, while the system can only be operated when $\eta_{STH} > 0$, (ii) the inert gas stream of N_2 required for SG and SG + EOP operation is generated via PV powered ITM SEOS unit, eliminating reliance on bottled gases and enhancing system autonomy, (iii) a fixed cycle time of 15 minutes for both reduction and oxidation phases was applied, consistent with experimental practice and necessary to maintain optimal EOP operating temperatures to avoid EOP structure destruction, and (iv) each method is assumed to operate at its corresponding $\eta_{STF,\ max}$ as determined by the predictive performance model.

The system also designed two heat recovery parts including the gas and the solid heat recovery parts. In the upstream process, the separated nitrogen was preheated by the outlet gas of the reduction reactor. The exhausted hot gas leaving the oxidation reactor passed through a counter-current gas-to-gas heat exchanger, where it transfers sensible heat across a solid wall to the cold CO_2 feed. The two streams did not mix and only heat was exchanged, then the preheated CO_2 entered the oxidation reactor, while the cooled exhaust proceeded to downstream handling. No external heat-transfer fluid (HTF) or thermal-energy storage (TES) loop is involved. The exchanger performance is referenced by the gas heat recovery coefficient (ε_g= 0.95). For the solid heat recuperation, it was implemented with a solid heat shuttle (a kind of mechanical solid regenerator) operating between two parts of reticulated porous ceria in different

thermochemical reactors (reactor 1 and reactor 2). An inert, high-thermal-conductivity solid element (alumina) alternately contacted the reactor in the reduction and the reactor in the oxidation: it absorbed sensible heat from the hot reduced ceria at reduction temperature is mechanically transferred, and then released that heat to the re-oxidized RPC at the low temperature when shifting the concentrated solar energy, and then the cycle repeated at next cycle. Performance was parameterized by the solid heat recovery coefficient ε_s which was consistent with that used in the prediction model (ε_s = 0.7) defined relative to the maximum recoverable sensible heat of the ceria (see Equation S1-2 in Section S1.1).

The annual fuel price (FP_{CO}) was utilized to compare the fuel production performance under different oxygen removal methods in this 500 kW level system defined by the total fuel produced and the annual investment:

$$FP_{CO}=\frac{C_{annual,\ total}}{FG_{CO}} \tag{S9-1}$$

where FG_{CO} is the annual CO generation depending on weather conditions and heliostat design, $C_{annual,\ total}$ is the annual total investment defined by the total plant investment (C_{total}) over the thermochemical system operation lifetime (t_{life} = 25 years) and the bank interest (i = 5%) defined as:[16]

$$C_{annual,\ total}=\frac{i\times(1+i)^{t_{life}}\times C_{total}}{(1+i)^{t_{life}}+1} \tag{S9-2}$$

where C_{total} is the initial investment for the thermochemical fuel production system.

C_{total} consists of 5 parts which are direct investment ($C_{D,\ total}$), indirect investment ($C_{Ind,\ total}$), contingency investment (C_{Cont}), maintenance cost (C_{Maint}), and feed cost (C_{Feed}) defined as:

$$C_{total}=C_{D,\,total}+C_{Ind,\,total}+C_{Cont}+C_{Maint}+C_{Feed} \quad \text{(S9-3)}$$

S9.2 Direct investment of system

The direct investment of the thermochemical fuel production system ($C_{D,\,total}$) consists of 5 parts which are the PV system (C_{PV}), heliostat investment (C_{Helio}), solar tower investment (C_{SolT}), reactor investment ($C_{Reactor}$), and land investment (C_{Land}), defined as:

$$C_{D,\,total}=C_{PV}+C_{Helio}+C_{SolT}+C_{Reactor}+C_{Land} \quad \text{(S9-4)}$$

S9.2.1 PV system investment (C_{PV})

Based on the assumption in Section 9.1, all the electricity is provided by the PV array separated into two parts a) for separating the inert gas from the air and b) for driving the pump (VP in SG + VP method and EOP in SG + EOP method). Hence, the total power of the PV system ($P_{PV,\,total}$) is defined by two parts: *i*) $P_{PV,\,Gas}$ the PV power for providing electricity which separates the inert gas from the air, and *ii*) $P_{PV,\,Pump}$ the power for providing electricity that drives the pump. $P_{PV,\,total}$ defined as:

$$P_{PV,\,Total}=P_{PV,\,Gas}+P_{PV,\,Pump} \quad \text{(S9-5)}$$

(1) $P_{PV,\,Gas}$ design

The energy required for separating the inert gas from air (q_{Gas}, J mol^{-1}) is decided by the thermochemical operation $p_{O2,\,red}$ which is defined as[17]:

$$q_{Gas}=\begin{cases}12000 & P_{O_2,\,red}<5\times10^{-4}\ \text{atm}\\ \ln\left(\dfrac{P_{O_2,\,air}}{P_{O_2,\,red}}\right)^2\times1000 & P_{O_2,\,red}\geq5\times10^{-4}\ \text{atm}\end{cases} \quad \text{(S9-6)}$$

while $P_{O2,\,air}$ is the oxygen partial pressure of the air, $P_{O_2,\,air}$ = 0.21 atm, and $P_{O_2,\,red}$ is

in consistent with the optimized P_{O_2} for each oxygen removal method, thus $P_{O_2,\,red}$ was 1.0×10^{-3} atm in the SG method, 5.01×10^{-4} atm in the SG + VP method, and 6.31×10^{-5} atm in the SG + EOP method.

As the two alternating thermochemical reactors continuously require N_2 for sweeping the ceria, the required $P_{PV,\,Gas}$ is defined as:

$$P_{PV,\,Gas} = \frac{q_{Gas} M_{N_2}}{DNI(t)_{min,\,valid} t_{Red} \eta_{STE}} \tag{S9-7}$$

Where M_{N_2} is the total N_2 in moles removed in each cycle depending on $P_{O_2,\,red}$, $DNI(t)_{min,valid}$ is the minimum valid DNI to drive the thermochemical reaction, as the PV array and the heliostat operate simultaneously, t_{Red} is the time duration of reduction, t_{Red} = 900 s, which is a reasonable value for heliostat-scale thermochemical reactor.[18]

(2) $P_{PV,\,Pump}$ design

For the SG method, $P_{PV,\,Pump}$ is 0 m^2 as the pump is not utilized. For the VP in the SG + VP method, the energy required per cycle is decided by the P_{VP} (see details in Section S1). As the VP was driven by the PV array which utilizes the solar energy, the area of PV for driving the VP can be defined as:

$$P_{PV,\,VP} = \frac{Q_{VP}}{DNI(t)_{min,\,valid} t_{Red} \eta_{STE}} \tag{S9-8}$$

For the EOP in the SG & EOP method, the energy required is defined as:

$$P_{PV,\,EOP} = \frac{Q_{EOP}}{DNI(t)_{min,\,valid} t_{Red} \eta_{STE}} \tag{S9-9}$$

Thus, the C_{PV} is defined as:

$$C_{PV}=P_{PV,\,Total}c_{PV} \quad \text{(S9-10)}$$

where c_{PV} is the cost of PV, c_{PV} = 0.31 \$·W^{-1} for PV system.[19]

S9.2.2 Heliostat plant investment (C_{Helio})

The heliostat plant investment only consists of the expense of heliostats, and N_{Helio} can be seen in Fig S9-2F. The C_{Helio} is defined as:

$$C_{Helio}=c_{Helio}a_{Helio}N_{Helio} \quad \text{(S9-10)}$$

where a_{Helio} is the area of each heliostat, a_{Helio} = 2.25 m^2, c_{Helio} is the cost of heliostat per square meter, c_{Helio} = 140 \$·m^{-2}.[20]

S9.2.3 Solar tower investment (C_{SolT})

The C_{SolT} is mainly dependent on the height of the solar tower (H_{SolT}) and the total area of the heliostat (A_{Helio}) which is defined as: [16, 19]

$$C_{SolT}=4785H_{SolT}-10.51A_{Helio}+0.608H_{SolT}A_{Helio}-82740 \quad \text{(S9-11)}$$

The total area of the heliostat (A_{Helio}) is defined as:

$$A_{Helio}=N_{Helio}a_{Helio} \quad \text{(S9-12)}$$

S9.2.4 Reactor investment ($C_{Reactor}$)

The reactor receives the concentrated solar irradiation before transferring the solar energy into heat, which drives the thermochemical reaction, and the $C_{Reactor}$ is defined as:[21]

$$C_{\text{Reactor}} = 0.5224 P_{\text{Reactor, max}}^{0.93} \times 2 \quad \text{(S9-13)}$$

where $P_{\text{Reactor,max}}$ is the maximum solar heat received by the reactor, thus the designed reactor can satisfy the annual thermochemical reaction need.

$P_{\text{Reactor, max}}$ is defined as:

$$P_{\text{Reactor, max}} = P_{\text{Helio}} (\eta_{\text{optical}} \eta_{\text{STH}})_{\text{max}} \quad \text{(S9-14)}$$

where the η_{optical} is the optical efficiency of the heliostat plant and the η_{STH} is the solar-to-heat efficiency depending the hour-wise DNI (t), T_{red}, and the solar concentration ratio ($c_{\text{R}}(t)$) of the heliostat plant defined as:

$$\eta_{\text{STH}} = 1 - \frac{\sigma T_{\text{red}}^4}{DNI(t) c_{\text{R}}(t)} \quad \text{(S9-15)}$$

where σ is the Stefan-Boltzmann constant (5.67×10^{-8} W·m^{-2}·K^{-4}). In Yumen, the reactor was designed based on the $P_{\text{Reactor, max}}$ on the Summer Solstice for satisfying the fuel generation need each year. The reactor power was 25.93 kW for SG method, 30.43 kW for SG + VP method, and 34.21 kW for SG + EOP method. Based on earlier research conducted by researchers in ETH who implemented a 50 kW reactor,[18] we adopted a geometrically similar scale-down of the ETH reactor by a linear factor s ($s = P_{\text{Reactor, max}}/50$). All lengths scaled as s, areas as s^2, and volumes/masses as s^3. To preserve physics, we kept the ceria porosity and optical thickness. The total molar CO_2 and N_2 was decided based on the P_{O_2} and $\eta_{\text{STF, max}}$ at fixed volumetric flow rate. In the SG + EOP configuration, the required EOP active area scales linearly with the ceria inventory (2.826×10^{-3} m^2 per mole). To limit current per device, the EOP was modularized into identical units (2.826×10^{-3} m^2 each). The module count per reactor was set by the ceria loading in reactor operating in different oxygen removal methods. For heat management, the surface/volume ratio grows as $1/s$, so radiative/conductive

losses become relatively larger; we compensate by improved insulation/window sealing and by keeping gas/solid heat recovery in the reaction implying exchanger areas s^2 and recuperator residence time preserved at fixed superficial velocity. This strategy yields a dynamically and optically similar miniature reactor while highlighting the expected penalty of higher relative losses at small scale and the required mitigations.

S9.2.5 Land investment (C_{Land})

The land investment of the required PV array and heliostat plant areas is calculated by considering a land use factor of 0.35 and land unit cost of 2 $\$\cdot m^{-2}$ which is defined as:[22]

$$C_{Land}=\frac{2\times(A_{PV,\,Total}+A_{Helio})}{0.35} \tag{S9-16}$$

S9.3 Indirect investment of the system

The indirect investment can be separated into 2 parts, which are the heliostat part ($C_{Ind,\,Helio}$) and the other parts ($C_{Ind,\,Other}$):

$$C_{Ind,\,Total}=C_{Ind,\,Helio}+C_{Ind,\,Other} \tag{S9-17}$$

The $C_{Ind,\,Helio}$ is calculated by considering a use factor of 0.1, which is defined as:[22]

$$C_{Ind,\,Helio}=0.1C_{Helio} \tag{S9-18}$$

And the rest is defined by other the parts of $C_{D,\,Total}$ by considering a factor of 0.2:[22]

$$C_{Ind,\,Other}=0.2(C_{D,total}-C_{Helio}) \tag{S9-19}$$

S9.4 Contingency investment (C_{Cont})

A 15% contingency cost for the whole system, C_{Cont}, is added to the $C_{D.\,Total,}$ which can

be defined as:[16]

$$C_{\mathrm{Cont}}=0.15C_{\mathrm{D,total}} \quad \text{(S9-20)}$$

S9.5 Maintenance investment (C_{Maint})

C_{Maint} is included for operating the system and assumed as equal to 4% of $C_{\mathrm{D.\ Total}}$, which can be defined as:[16]

$$C_{\mathrm{Maint}}=0.04C_{\mathrm{D,\ Total}} \quad \text{(S9-21)}$$

S9.6 Feed investment (C_{Feed})

CO_2 is reduced to CO in the thermochemical system which is the feed gas. The C_{Feed}, is based on a specific commercial cost of 0.1808 \$·kg^{-1} and multiplied by the quantity required over the lifetime (25 years):[23]

$$C_{\mathrm{feed}}=N_{\mathrm{annual},CO_2}M_{CO_2}t_{\mathrm{life}} \quad \text{(S9-22)}$$

Where the $N_{\mathrm{annual,\ CO_2}}$ is the annual required CO_2, the same as the annual required CO ($N_{\mathrm{annual,\ CO}}$). M_{CO_2} is the molecular weight of CO_2 (44 g·mol^{-1}).

$N_{\mathrm{annual,\ CO}}$ is defined as:

$$N_{\mathrm{Annual,\ CO}}=\sum N_{Season,\ \mathrm{CO}} \quad \text{(S9-23)}$$

where the subscript *Season* represents Spring, Summer, Autumn, and Winter.

$$N_{Season,\,\mathrm{CO}} = FG_{\mathrm{CO}} \sum_{t_{\mathrm{Start,\,hour}}}^{t_{\mathrm{End,\,hour}}} \frac{t_{\mathrm{cycle}} P_{\mathrm{Helio}} \eta_{\mathrm{optical}}(t) \eta_{\mathrm{STH}}(t) \eta_{\mathrm{STF,\,max}}}{\Delta H_{\mathrm{CO}}} N_{\mathrm{cycle}} N_{Season} \quad \text{(S9-24)}$$

Where $t_{\mathrm{Start,hour}}$ and $t_{\mathrm{End,\,hour}}$ are the starting and end hours, $\eta_{\mathrm{optical}}(t)$ and $\eta_{\mathrm{STH}}(t)$ are the hour-wise optical efficiency and solar to heat efficiency of the heliostat field, N_{cycle} is the daily number of cycles in each season depending on the total operation hours, N_{Season} is the number of days in each season, and $\eta_{\mathrm{STF,\,max}}$ is the maximum η_{STF} of each oxygen removal method.

The cost constituent of each part can thus be defined as:

$$f_{FP_i} = \frac{FP_i}{FP_{\mathrm{CO}}} \quad \text{(S9-25)}$$

where the subscript *i* indicates different parts of the investment.

S9.7 Heliostat plant design

The design of the heliostat plant was based on η_{optical}, accounting for spillage, cosine, shading/blocking, and transmission losses as a function of solar position and site location. The total number of the ray used in this model was 2×10^9 in each case. A mature and commercially deployed heliostat structure from *BCP Solar Technology* was adopted as the reference design. The design point is at solar noon on the Summer Solstice for cities except Alice Springs, whose design point is Winter Solstice, as a city in the southern hemisphere.

S9.7.1 Solar tower height optimization

A parametric study optimized the heliostat tower height (H_{SolT}) for higher η_{optical}. The H_{SolT} was optimized through parametric analysis to maximize η_{optical} at solar noon on the Summer Solstice in Yumen. The desired number of ray intersections is 2×10^7 and

the maximum of generated rays is 2×10^9. The H_{SolT} varied from 5 m to 30 m and was conducted for other locations using identical operation conditions, with results summarized in Fig. S9-1.

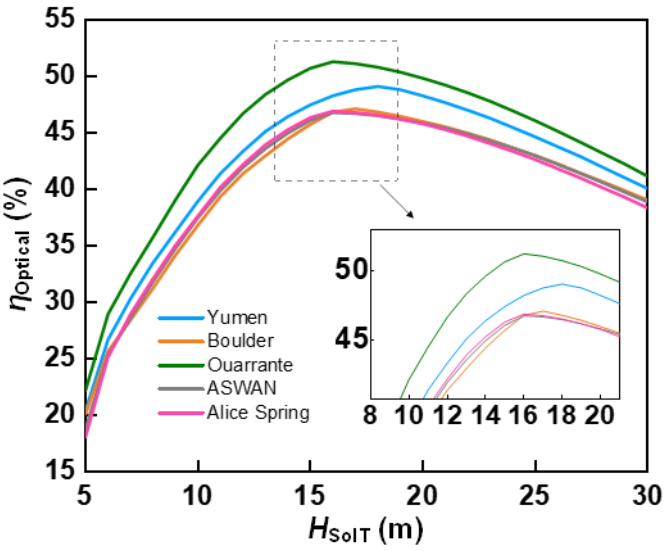

Fig S9-1. $\eta_{optical}$ as a function of H_{SolT} in different locations: (a) Yumen, (b) Boulder, (c) Ouarzazate, (d) Aswan, (e) Alice Springs.

The optimized H_{SolT} was 18 m for Yumen, 17 m for Boulder, 16 m for Ouarzazate, 16 m for Aswan, and 16 m for Alice Springs.

S9.7.2 Heliostat distribution in the plant

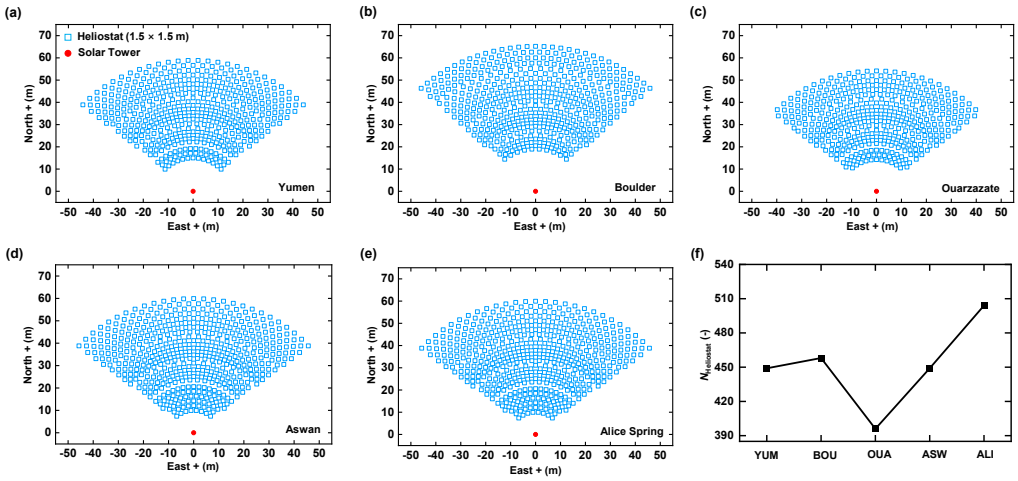

Fig S9-2. The heliostat plant design of different locations. (A) Yumen (B) Boulder (C) Ouarzazate (D) Aswan (E) Alice Springs (F) N_{Helio} of heliostat plant in different locations. YUM (Yumen), BOU (Boulder), OUA (Ouarzazate), ASW (Aswan), ALI: Alice Springs.

S9.8 Environmental and heliostat operation conditions

To capture seasonal variation, four representative days, including Spring Equinox, Summer Solstice, Autumn Equinox, and Winter Solstice, were selected. The average hourly DNI on each day was calculated using the mean of the two adjacent days before and after the target date. This approach provided a representative hourly solar input profile for system performance simulations across the year.

S9.8.1 Yumen results

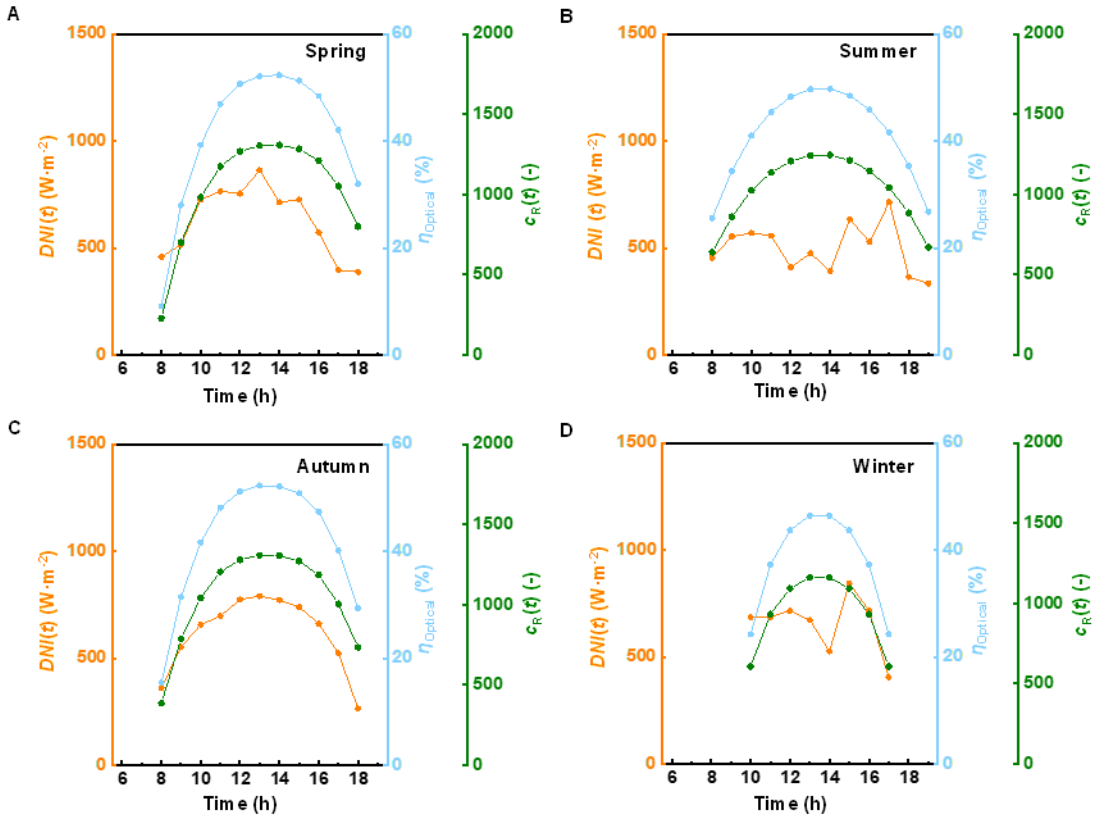

Fig S9-3. $DNI(t)$ (left y-axis, orange axis), $\eta_{optical}$ (right y-axis, blue axis), and $c_R(t)$ (right y-axis, green axis) as a function of time in Yumen. Results of different seasons: (A) spring, (B) summer, (C) autumn, (D) winter.

S9.8.2 Boulder results

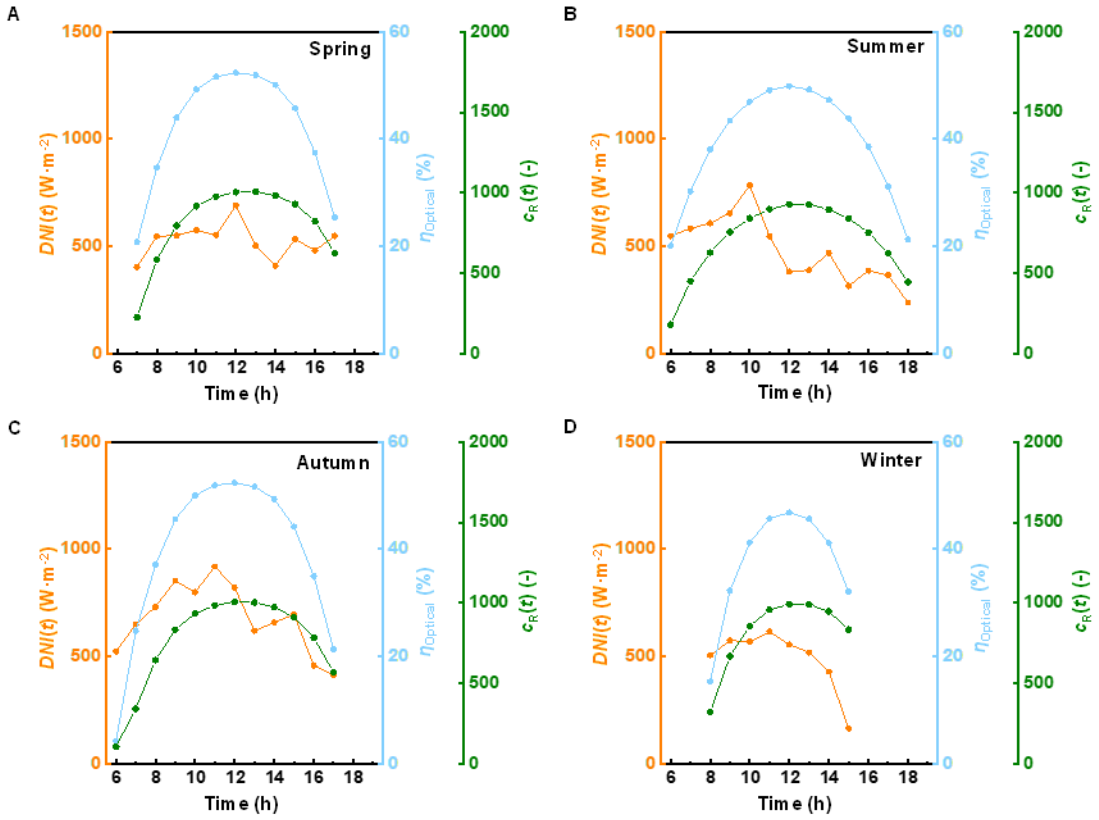

Fig S9-4. $DNI(t)$ (left y-axis, orange axis), $\eta_{optical}$ (right y-axis, blue axis), and $c_R(t)$ (right y-axis, green axis) as a function of time in Boulder. Results of different seasons: (A) spring, (B) summer, (C) autumn, (D) winter.

S9.8.3 Ouarzazate results

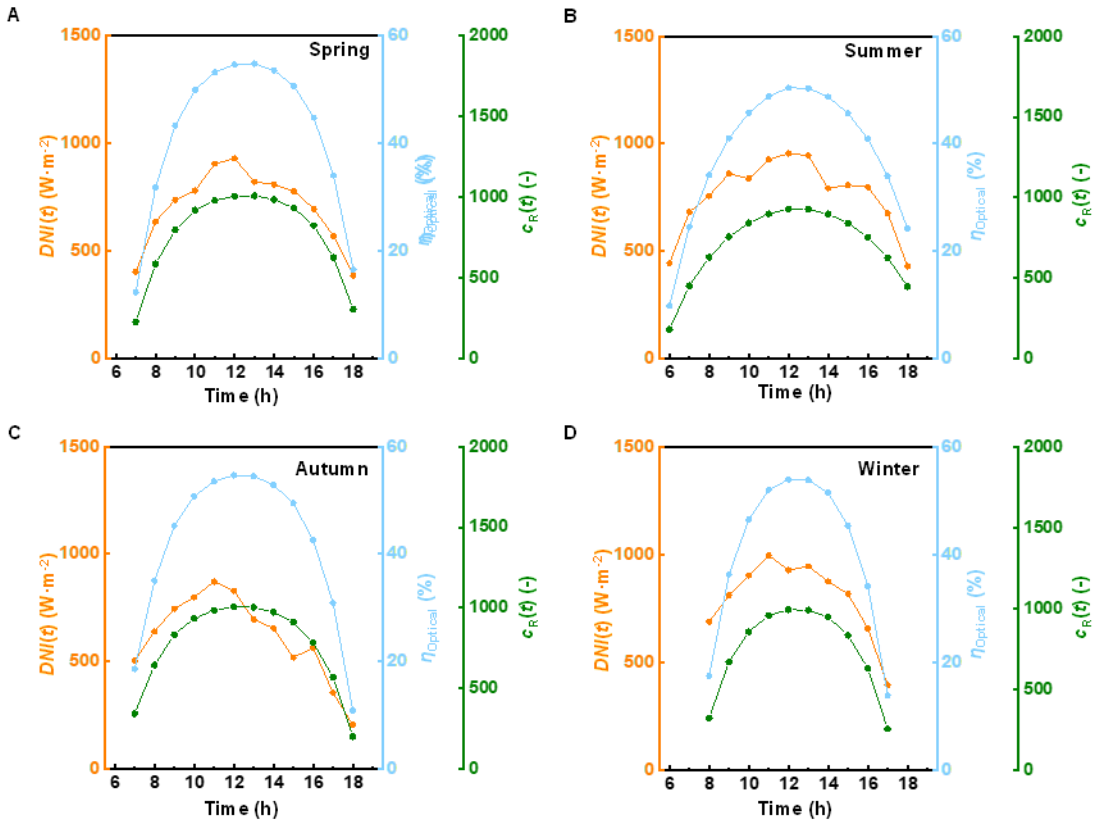

Fig S9-5. $DNI(t)$ (left y-axis, orange axis), $\eta_{optical}$ (right y-axis, blue axis), and $c_R(t)$ (right y-axis, green axis) as a function of time in Ouarzazate. Results of different seasons: (A) spring, (B) summer, (C) autumn, (D) winter.

S9.8.4 Aswan results

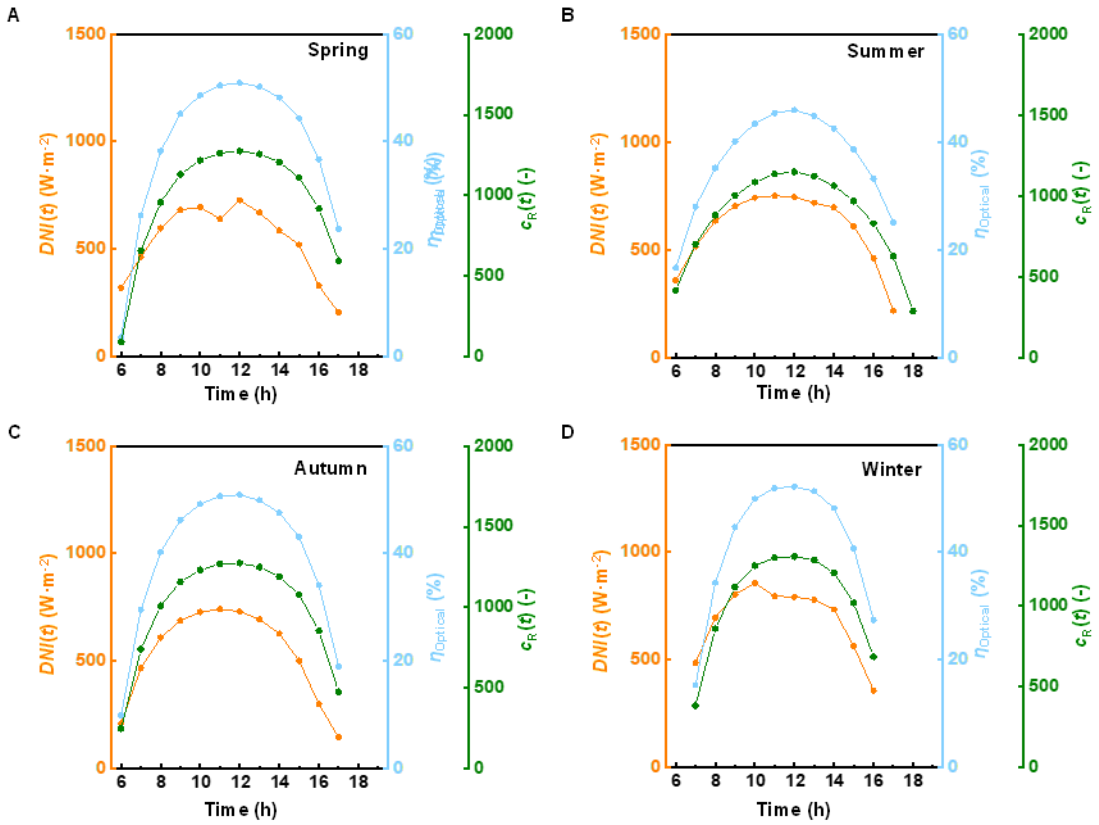

Fig S9-6. $DNI(t)$ (left y-axis, orange axis), η_{optical} (right y-axis, blue axis), and $c_R(t)$ (right y-axis, green axis) as a function of time in Aswan. Results of different seasons: (A) spring, (B) summer, (C) autumn, (D) winter.

S9.8.5 Alice Springs results

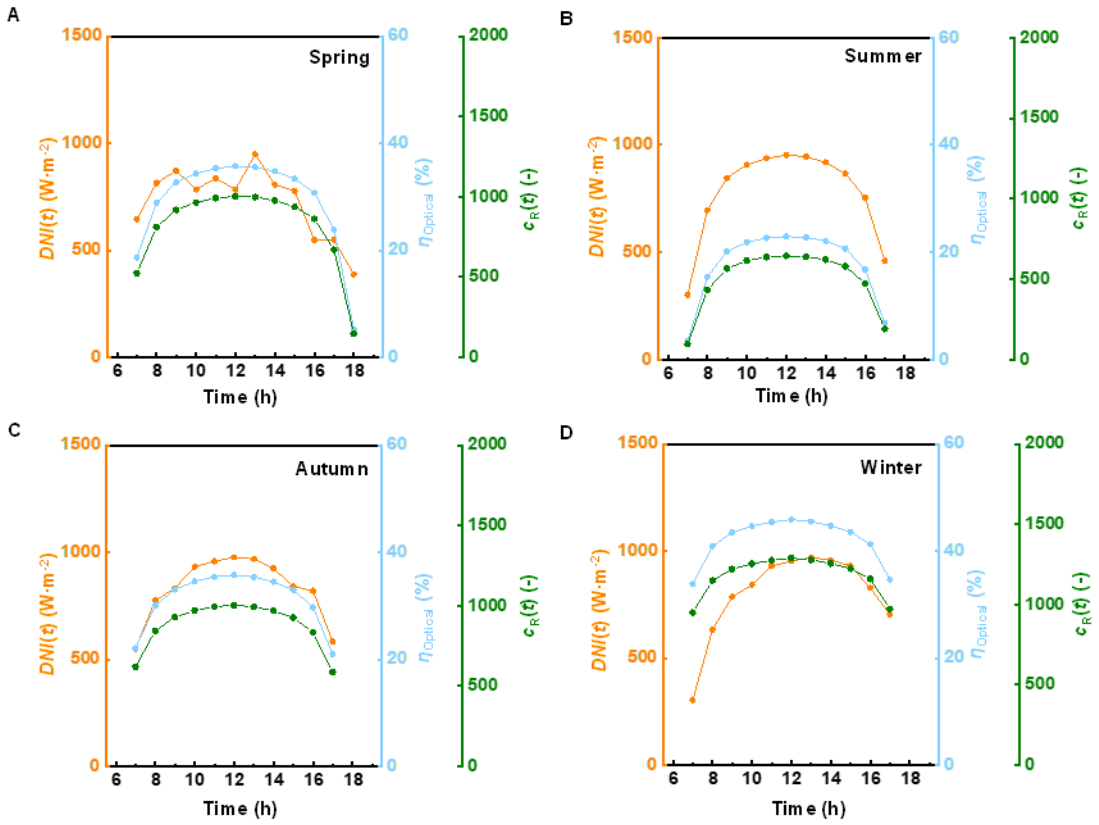

Fig S9-7. $DNI(t)$ (left y-axis, orange axis), $\eta_{optical}$ (right y-axis, blue axis), and $c_R(t)$ (right y-axis, green axis) as a function of time in Alice Springs. Results of different seasons: (A) spring, (B) summer, (C) autumn, (D) winter.

S9.8 Local Effects

Location factors strongly influence fuel yield, as higher DNI enhances the thermal input available to drive endothermic reactions, and the local capacities are shown in Table S9-1 and the local effects on the FC_{CO} under different oxygen removal methods at $\eta_{STF,max}$ can be seen in Figure S9-8.

Table S9-1 Calculated capacities for thermochemical fuel system at different sites

Calculated capacities	Yumen	Boulder	Ouarz-azate	Aswan	Alice Springs
Annual total DNI ($kWh \cdot m^{-2} \cdot year^{-1}$)	2324	1681	2116	1849	2324
Annual solar-to-fuel efficiency (%)	17.69% (SG method, 1.0×10^{-3} atm) 21.07% (SG & VP method, 5.01×10^{-4} atm) 23.69% (SG & EOP method, 6.31×10^{-5} atm)				
Designed Heliostat plant power, P_{Helio} (kW)	588.0	458.0	432.1	587.2	660.0
Maximum optical efficiency, $\eta_{optical}$ (%)	52.32	49.23	54.71	52.23	45.89
Maximum solar-to-heat efficiency, η_{STH} (%)	46.94	41.91	41.19	47.67	54.78
Annual valid operating hours ($h \cdot year^{-1}$)	2821	2148	2548	2639	2821

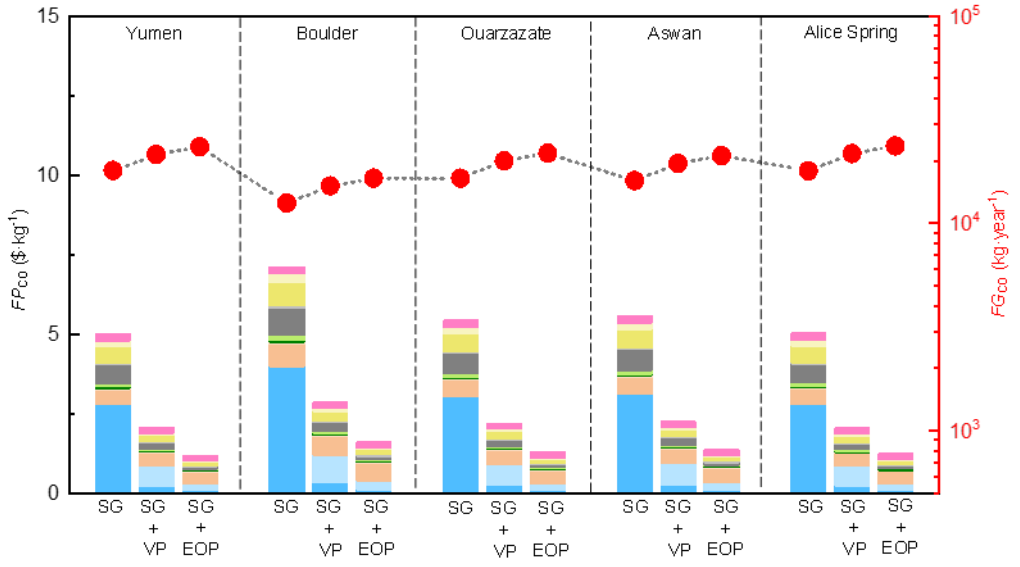

Figure S9-8. Local effects on both the FP_{CO} (left y-axis) and FG_{CO} (right y-axis) under 3 oxygen removal methods. Locations from left to right: Yumen (China, Asia), Boulder (USA, North America), Ouarzazate (Morocco, Africa), Aswan (Egypt, Africa), and

Alice Springs (Australia, Oceania).

Table S9-1 summarizes the site-specific solar resource and plant design parameters. The annual total DNI varies significantly across the selected sites, from 1681 kWh·m^{-2}·year^{-1} in Boulder to 2324 kWh·m^{-2}·year^{-1} in Yumen and Alice Springs. This variation directly translates into different designed heliostat capacities and valid operating hours. As shown in Figure S9-8, these site-dependent capacities strongly influence the economics of CO production. Locations with higher DNI not only reduce the unit cost of CO but also enable higher annual production. In Yumen, the FP_{CO} was 1.19 \$·kg^{-1} under SG+EOP with an output of 2.33 × 10^4 kg·year^{-1}, whereas in Boulder, the lower solar resource raises costs and limits production despite using the same configuration. Across all sites, SG + EOP consistently delivers the lowest FP_{CO} and the highest yield compared with SG and SG + VP, confirming that both the oxygen removal method and the local solar resource jointly dictate the techno-economic feasibility of large-scale deployment.

S9.9 Future Cost

PV module and heliostat costs can be predicted using Wright's law with a 0.2 learning rate (LR) for PV[24] and a reasonable learning rate (LR = 0.2) for heliostat based on technology development,[26, 27] which are based on the present base cost ($fc_{x,0}$) and future cumulative capacity ($FCC_x(t)$) defined as:

$$fc_x(t)=fc_{x,0}\left[\frac{FCC_x(t)}{FCC_x(t_0)}\right]^{-b} \quad \text{(S9-26)}$$

$$b=-\log_2(1\text{-LR}) \quad \text{(S9-27)}$$

where the subscript x denotes to PV or heliostat technology, t_0 is the base time, $fc_x(t)$ is the technology future cost, $FCC_x(t_0)$ is the base cumulative capacity technology,

and $FCC_x(t)$ is the future cumulative capacity technology. The future cost prediction does not apply the learning rate to ITM SEOS, tower/receiver/reactor, land, or indirect (held constant in real terms) costs.

The IEA reports heliostat totals only for 2030 and 2050, the heliostat cumulative capacity is constructed by piecewise-linear interpolation between the 2025 baseline, the 2030 target, and the 2050 outlook.[27] The PV cumulative-capacity trajectory follows the scenario shown in Figure S9-9A.[28] The future cost of both PV and the heliostat based on the predicted cumulative capacity can be seen in Figure S9-10. Under this policy, SG and SG+VP methods remain PV price sensitive, whereas SG + EOP requires less PV electricity for in-situ deoxygenation as it shifts cost sensitivity toward the heliostat field which can be seen in Figure 4D.

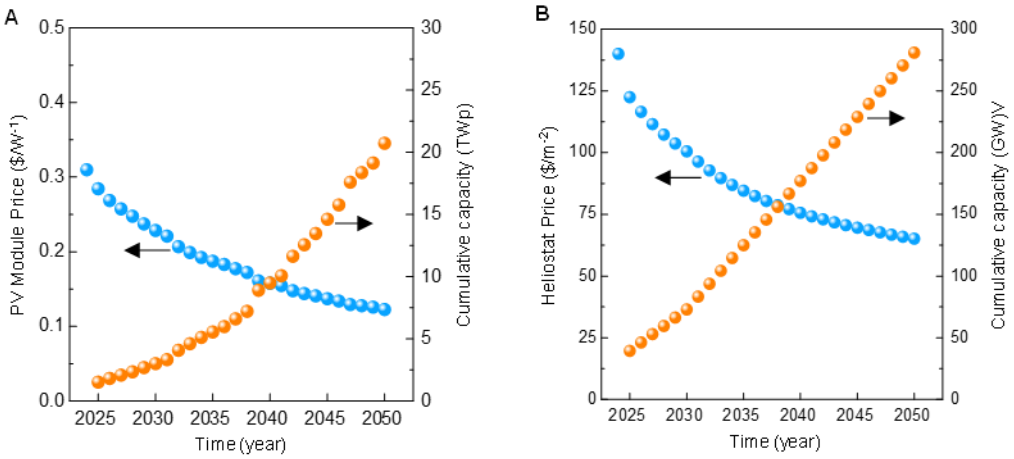

Figure S9-9. Future Price (left y-axis) and predicted cumulative capacity of (A) PV module and (B) Heliostats.

References

1. Jarrett, C., Chueh, W., Yuan, C., Kawajiri, Y., Sandhage, K.H., and Henry, A. (2016). Critical limitations on the efficiency of two-step thermochemical cycles. Solar Energy *123*, 57–73. https://doi.org/10.1016/j.solener.2015.09.036.
2. Lidor, A., and Bulfin, B. (2024). A critical perspective and analysis of two-step thermochemical fuel production cycles. Solar Compass *11*, 100077. https://doi.org/10.1016/j.solcom.2024.100077.
3. Lin, M., and Haussener, S. (2015). Solar fuel processing efficiency for ceria redox cycling using alternative oxygen partial pressure reduction methods. Energy *88*, 667–679. https://doi.org/10.1016/j.energy.2015.06.006.
4. Huang, H., and Lin, M. (2022). Dynamic behavior of solar thermochemical reactors for fuel generation: Modeling and control strategies. Energy Conversion and Management *270*, 116232. https://doi.org/10.1016/j.enconman.2022.116232.
5. Bai, W., Huang, H., Suter, C., Haussener, S., and Lin, M. (2022). Enhanced Solar-to-Fuel Efficiency of Ceria-Based Thermochemical Cycles via Integrated Electrochemical Oxygen Pumping. ACS Energy Lett. *7*, 2711–2716. https://doi.org/10.1021/acsenergylett.2c01318.
6. Ni, M., Leung, M., and Leung, D. (2007). Parametric study of solid oxide steam electrolyzer for hydrogen production. International Journal of Hydrogen Energy *32*, 2305–2313. https://doi.org/10.1016/j.ijhydene.2007.03.001.
7. Reid, R.C., Prausnitz, J.M., and Poling, B.E. (1987). The properties of gases and liquids 4th ed. (McGraw-Hill).
8. Veldsink, J.W., Van Damme, R.M.J., Versteeg, G.F., and Van Swaaij, W.P.M. (1995). The use of the dusty-gas model for the description of mass transport with chemical reaction in porous media. The Chemical Engineering Journal and the Biochemical Engineering Journal *57*, 115–125. https://doi.org/10.1016/0923-0467(94)02929-6.
9. Ferguson, J.R., Fiard, J.M., and Herbin, R. (1996). Three-dimensional numerical simulation for various geometries of solid oxide fuel cells. Journal of Power Sources *58*, 109–122. https://doi.org/10.1016/0378-7753(95)02269-4.
10. Lidor, A., Aschwanden, Y., Häseli, J., Reckinger, P., Haueter, P., and Steinfeld, A. (2023). High-temperature heat recovery from a solar reactor for the thermochemical redox splitting of H_2O and CO_2. Applied Energy *329*, 120211. https://doi.org/10.1016/j.apenergy.2022.120211.
11. Suwanwarangkul, R., Croiset, E., Entchev, E., Charojrochkul, S., Pritzker, M.D., Fowler, M.W., Douglas, P.L., Chewathanakup, S., and Mahaudom, H. (2006). Experimental and modeling study of solid oxide fuel cell operating with syngas fuel. Journal of Power Sources *161*, 308–322. https://doi.org/10.1016/j.jpowsour.2006.03.080.
12. Ackermann, S., Takacs, M., Scheffe, J., and Steinfeld, A. (2017). Reticulated porous ceria undergoing thermochemical reduction with high-flux irradiation.

International Journal of Heat and Mass Transfer *107*, 439–449. https://doi.org/10.1016/j.ijheatmasstransfer.2016.11.032.
13. Chase, M. (1998). NIST-JANAF thermochemical tables 4th ed. (American chemical society).
14. Panlener, R.J., Blumenthal, R.N., and Garnier, J.E. (1975). A thermodynamic study of nonstoichiometric cerium dioxide. Journal of Physics and Chemistry of Solids *36*, 1213–1222. https://doi.org/10.1016/0022-3697(75)90192-4.
15. Marxer, D., Furler, P., Takacs, M., and Steinfeld, A. (2017). Solar thermochemical splitting of CO_2 into separate streams of CO and O_2 with high selectivity, stability, conversion, and efficiency. Energy Environ. Sci. *10*, 1142–1149. https://doi.org/10.1039/C6EE03776C.
16. Lin, M., and Haussener, S. (2017). Techno-economic modeling and optimization of solar-driven high-temperature electrolysis systems. Solar Energy *155*, 1389–1402. https://doi.org/10.1016/j.solener.2017.07.077.
17. Li, S., Wheeler, V.M., Kumar, A., Venkataraman, M.B., Muhich, C.L., Hao, Y., and Lipiński, W. (2022). Thermodynamic Guiding Principles for Designing Nonstoichiometric Redox Materials for Solar Thermochemical Fuel Production: Ceria, Perovskites, and Beyond. Energy Tech *10*, 2000925. https://doi.org/10.1002/ente.202000925.
18. Zoller, S., Koepf, E., Nizamian, D., Stephan, M., Patané, A., Haueter, P., Romero, M., González-Aguilar, J., Lieftink, D., De Wit, E., et al. (2022). A solar tower fuel plant for the thermochemical production of kerosene from H2O and CO2. Joule *6*, 1606–1616. https://doi.org/10.1016/j.joule.2022.06.012.
19. Barbose, G.L., Darghouth, N.R., O'Shaughnessy, E., and Forrester, S. (2024). Tracking the Sun: Pricing and Design Trends for Distributed Photovoltaic Systems in the United States, 2024 Edition. Lawrence Berkeley National Laboratory.
20. Kurup, P., Turchi, C., Akar, S., Glynn, S., Augustine, C., and Davenport, P. (2022). Cost Update: Commercial and Advanced Heliostat Collectors. National Renewable Energy Laboratory (NREL).
21. Singer, C., Buck, R., Pitz-Paal, R., and Müller-Steinhagen, H. (2010). Assessment of Solar Power Tower Driven Ultrasupercritical Steam Cycles Applying Tubular Central Receivers With Varied Heat Transfer Media. Journal of Solar Energy Engineering *132*, 041010. https://doi.org/10.1115/1.4002137.
22. Meier, A., Gremaud, N., and Steinfeld, A. (2005). Economic evaluation of the industrial solar production of lime. Energy Conversion and Management *46*, 905–926. https://doi.org/10.1016/j.enconman.2004.06.005.
23. Fu, Q., Mabilat, C., Zahid, M., Brisse, A., and Gautier, L. (2010). Syngas production via high-temperature steam/CO2 co-electrolysis: an economic assessment. Energy Environ. Sci. *3*, 1382. https://doi.org/10.1039/c0ee00092b.
24. De La Tour, A., Glachant, M., and Ménière, Y. (2013). Predicting the costs of photovoltaic solar modules in 2020 using experience curve models. Energy *62*, 341–348. https://doi.org/10.1016/j.energy.2013.09.037.

25. Zhu, G., Augustine, C., Glatzmaier, G. (2022). Roadmap to Advance Heliostat Technologies for Concentrating Solar-Thermal Power. National Renewable Energy Laboratory (NREL).
26. Pidaparthi, A. (2017). Heliostat Cost Reduction for Power Tower Plants. https://doi.org/10.13140/RG.2.2.36064.69129.
27. Bouckaert, S., Fernandez Pales, A., McGlade, C., Remme, U., Wanner, B., Varro, L., D'Ambrosio, D., and Spencer, T. (2021). Net Zero by 2050: A Roadmap for the Global Energy Sector. International Energy Agency, Paris.
28. Vartiainen, E., Breyer, C., Moser, D., Román Medina, E., Busto, C., Masson, G., Bosch, E., and Jäger-Waldau, A. (2022). True Cost of Solar Hydrogen. Solar RRL *6*, 2100487. https://doi.org/10.1002/solr.202100487.